AGU PUBLICATIONS

JGR

Journal of Geophysical Research: Atmospheres

RESEARCH ARTICLE
10.1002/2016JD026328

Key Points:
- Bulk and surface chemical characterization of nine different volcanic ash particle samples covering wide silica range
- Microphysical properties including particle DRE mass density and shape characterization
- Hyperspectral complex refractive indices in UV/Vis/NIR range

Supporting Information:
- Data Set S1
- Data Set S2
- Data Set S3
- Data Set S4
- Data Set S5
- Data Set S6
- Data Set S7
- Data Set S8
- Data Set S9
- Data Set S10
- Data Set S11
- Data Set S12
- Data Set S13
- Data Set S14
- Data Set S15
- Data Set S16

Correspondence to:
A. Vogel,
andreas.vogel@nilu.no

Citation:
Vogel, A., S. Diplas, A. J. Durant, A. S. Azar, M. F. Sunding, W. I. Rose, A. Sytchkova, C. Bonadonna, K. Krüger, and A. Stohl (2017), Reference data set of volcanic ash physicochemical and optical properties, *J. Geophys. Res. Atmos.*, *122*, 9485–9514, doi:10.1002/2016JD026328.

Received 5 DEC 2016
Accepted 2 AUG 2017
Accepted article online 4 AUG 2017
Published online 7 SEP 2017

Reference data set of volcanic ash physicochemical and optical properties

A. Vogel[1,2], S. Diplas[3,4], A. J. Durant[2,5], A. S. Azar[3], M. F. Sunding[3], W. I. Rose[5], A. Sytchkova[6], C. Bonadonna[7], K. Krüger[2], and A. Stohl[1]

[1]Atmosphere and Climate Department, Norwegian Institute for Air Research, Kjeller, Norway, [2]Department of Geoscience, Meteorology and Oceanography Section, University of Oslo, Oslo, Norway, [3]SINTEF Materials and Chemistry, Oslo, Norway, [4]Centre for Material Science and Nanotechnology, Department of Chemistry, University of Oslo, Oslo, Norway, [5]Geological and Mining Engineering and Sciences, Michigan Technological University, Houghton, Michigan, USA, [6]Energy Technologies Department, Optical Components Group, ENEA Casaccia C.R.E, Rome, Italy, [7]Department of Earth Sciences, University of Geneva, Geneva, Switzerland

Abstract Uncertainty in the physicochemical and optical properties of volcanic ash particles creates errors in the detection and modeling of volcanic ash clouds and in quantification of their potential impacts. In this study, we provide a data set that describes the physicochemical and optical properties of a representative selection of volcanic ash samples from nine different volcanic eruptions covering a wide range of silica contents (50–80 wt % SiO_2). We measured and calculated parameters describing the physical (size distribution, complex shape, and dense-rock equivalent mass density), chemical (bulk and surface composition), and optical (complex refractive index from ultraviolet to near-infrared wavelengths) properties of the volcanic ash and classified the samples according to their SiO_2 and total alkali contents into the common igneous rock types basalt to rhyolite. We found that the mass density ranges between $\rho = 2.49$ and 2.98 g/cm^3 for rhyolitic to basaltic ash types and that the particle shape varies with changing particle size ($d < 100$ μm). The complex refractive indices in the wavelength range between $\lambda = 300$ nm and 1500 nm depend systematically on the composition of the samples. The real part values vary from $n = 1.38$ to 1.66 depending on ash type and wavelength and the imaginary part values from $k = 0.00027$ to 0.00268. We place our results into the context of existing data and thus provide a comprehensive data set that can be used for future and historic eruptions, when only basic information about the magma type producing the ash is known.

1. Introduction

During explosive volcanic eruptions, volcanic ash (VA) particles can be released into the atmosphere and transported hundreds to thousands of kilometers away from the eruptive vent. Depending on the eruption conditions (e.g., height of release), atmospheric conditions, and microphysical properties of VA, the particles have atmospheric lifetimes that can span hours (sedimentation velocities of ~1 km/h for coarse ash particles, $d > 63$ μm) to days and months (~0.01 km/h for fine ash particles, $d < 63$ μm) [*Bonadonna et al.*, 1998; *Rose et al.*, 2001; *Durant*, 2015]. During their atmospheric long-range transport, VA particles have the potential to influence the Earth's radiation balance as they reflect and absorb solar and terrestrial radiation, and therefore, they may impact weather and climate [*Robock*, 2000; *Vernier et al.*, 2016]. They also present a major threat for aviation operations as they decrease visibility and cause dangerous airframe and engine damages [*Prata and Tupper*, 2009; *Guffanti et al.*, 2010]. Near the Earth surface VA particles pose hazards to human health [*Baxter et al.*, 2014], affect air quality [*Thorsteinsson et al.*, 2012], infrastructures such as ground transport and water supplies [*Wilson et al.*, 2012], and to natural environments [*Jones and Gislason*, 2008; *Durant et al.*, 2010].

Atmospheric models, such as particle transport and dispersion, radiative transfer, or climate models, and ash retrieval algorithms rely on accurate and quantitative information about the different properties of VA. These properties deviate greatly between different volcanic ash types as they depend on individual magma properties (e.g., composition, rheology, and gas content), the particle formation processes, and the distance from the eruptive vent (particle size). However, in most cases, models and measurement algorithms use only a single set of parameters for all types of eruptions. This oversimplification can introduce large uncertainties in calculations of the atmospheric dispersion or mass concentration calculations as these properties differ

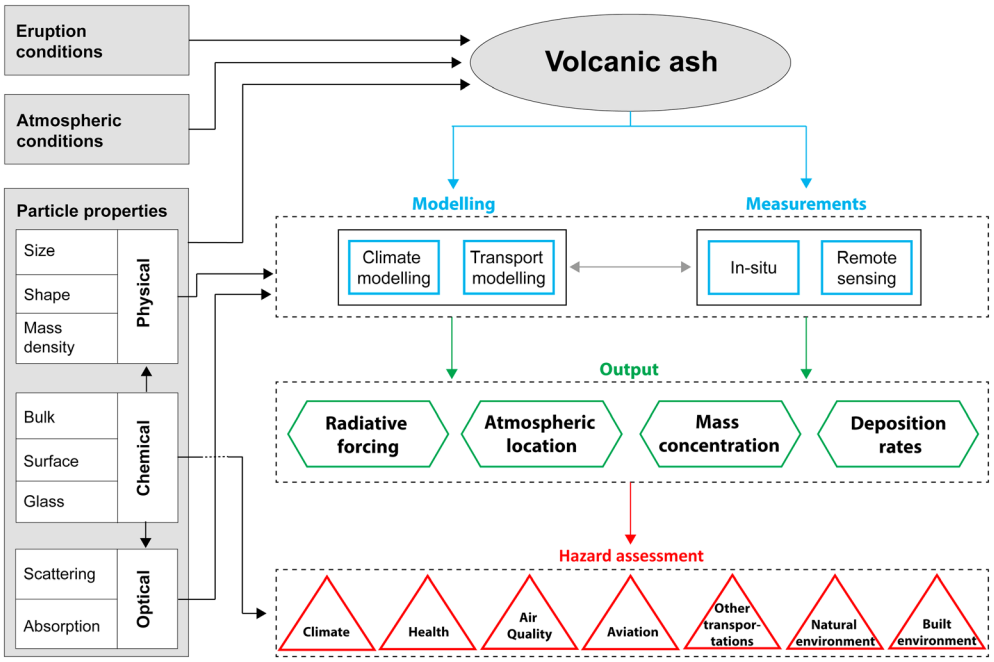

Figure 1. Flowchart illustrating how parameters describing the individual volcanic ash properties are needed for transport and dispersion as well as climate models and for ash measurement techniques. The chemical composition of the samples determines the mass density and the complex refractive index (RI) but also directly influences the severity of the ash's climate hazards, and its hazards for human health, air quality, and natural environment.

substantially from reality [*Grainger et al.*, 2013]. To minimize these uncertainties, there is an urgent need for more detailed and interrelated characterization of the properties of VA [*Rocha-Lima et al.*, 2014].

Figure 1 shows an overview about the main volcanic ash properties subdivided into chemical (mineralogical and chemical compositions of particle bulk and surface), physical (particle size, morphology, and mass density), and optical (complex refractive index) properties of VA. Accurate parameters describing these properties are needed in atmospheric dispersion and climate models as well as in remote sensing and in situ detection algorithms to provide reliable output products such as deposition rates, mass concentrations, and radiative forcing that are vital in the assessment of VA hazards.

1.1. Chemical Properties

The mineralogical and chemical compositions of VA are very complex and consist of glassy juvenile components, crystals from multiple mineral phases (quartz, feldspar, micas, pyroxenes, amphiboles, and olivine) formed in the magma, and lithic fragments of eroded vent and wall rock [*White and Houghton*, 2006; *Dingwell et al.*, 2012]. Typical VA composition ranges from basaltic (high in Mg and Fe) to rhyolitic (high in Si and Al) [*Stevenson et al.*, 2015] and is mostly described on the basis of the composition of the bulk material [*Bayhurst et al.*, 1994; *Weber et al.*, 2012; *Lieke et al.*, 2013], but can also be classified by the composition of the particle surface. The particle composition provides important information about the magma mixture and the erosion of the conduit rock [*Heiken*, 1972] and has an influence on scavenging processes in clouds and effects on the natural environment such as ocean and soil fertilization [*Duggen et al.*, 2009; *Achterberg et al.*, 2013]. The composition is also fundamental for deriving other VA properties such as the mass density or the complex refractive index.

The surfaces of the erupted VA particles represent a mixture of preeruptive, syneruptive, and posteruptive surfaces [*Ayris and Delmelle*, 2012]. Preeruptive surfaces are those generated at the boundaries between the silicate melts and the bubbles created during exsolution of magmatic volatiles [*Sparks*, 1978] and those generated by a permeable network of fractures [*Gonnermann and Manga*, 2003]. These surfaces are equilibrated via processes such as atomic rearrangement or ionic recombination. Syneruptive surfaces originate from the magma fragmentation in its brittle (solid-like) regime. Crystallization of mineral phases in silicate

melts introduces bulk material defects along phenocryst boundaries that act as fracture planes during magma fragmentation. As crystallization may involve diffusion of specific elements from the amorphous phase to the crystalline phase, fracture at the amorphous phase may generate surfaces depleted in the elements that were diffused into the crystalline phases. Posteruptive surfaces are generated by collision between ash particles or between particles and conduit wall rock after magma fragmentation. Ash particle surfaces are also influenced by high- and low-temperature heterogeneous chemical reactions in the eruption plume. Further, physical processes (e.g., adsorption and aggregation) and chemical reactions (e.g., leaching) occur during transport of the ash in the atmosphere. Both the bulk and surface compositions of VA particles have impacts on cloud microphysical processes [*Durant et al*., 2008; *Rolf et al*., 2012], radiative forcing [*Flanner et al*., 2014], respiratory effects [*Horwell and Baxter*, 2006], and soil and ocean fertilization effects [*Duggen et al*., 2009; *Achterberg et al*., 2013].

1.2. Physical Properties

Knowledge of the physical properties of VA particles is fundamental to constrain the size and style of volcanic eruptions [*Bonadonna and Houghton*, 2005] and to predict atmospheric lifetimes controlled by transport, deposition, and sedimentation processes [*Riley et al*., 2003; *Durant and Rose*, 2009; *Mills and Rose*, 2010; *Folch*, 2012; *Bagheri et al*., 2013]. Particle size and morphology are controlled by magma fragmentation processes [*Sparks*, 1978], magma ascent rate, and by external factors such as particle collisions or interaction with water [*Rose and Durant*, 2009; *Dellino et al*., 2012]. The deviation from spherical shape decreases atmospheric sedimentation velocities by up to 50% [*Mele et al*., 2011; *Bagheri and Bonadonna*, 2016a], due to the altered aerodynamic behavior of elongated particles. Thus, nonspherical particles can be transported over longer distances in the atmosphere than spherical particles [*Stevenson et al*., 2015; *Bagheri and Bonadonna*, 2016a].

To date, in measurement algorithms and atmospheric models, VA particles are often assumed to be spherical, although they are known to be nonspherical due to their formation processes [*Wilson and Huang*, 1979]. It has been shown that assuming mass-equivalent spheres instead of accounting for more realistically shaped porous nonspherical particles may lead to underestimates of the total retrieved mass of an ash cloud by approximately 30%. The assumption also leads to an overestimation of the ash cloud optical depth in radiative transfer algorithms that are used to interpret satellite measurement data [*Wen and Rose*, 1994; *Krotkov et al*., 1999b; *Kylling et al*., 2014]. *Bagheri and Bonadonna* [2016a], however, reported that even the most commonly used corrections for the estimation of nonspherical drag-coefficients (relevant for calculations of settling velocities) can introduce large errors (mean error up to 13% to maximum errors up to 80%) depending on the calculation method.

In another study, *Bagheri and Bonadonna* [2016a] reviewed commonly used nonspherical drag models for estimating VA particle drag coefficients and benchmarked them against analytical and experimental results. They showed that nonspherical drag models are on average associated with errors between 8% and 55% depending on the particle size (in the particle size of fine ash to lapilli-sized particles). The individual reported errors are 2–10% for fine ash, 23–55% for coarse ash, and 10–33% for lapilli-sized particles. Interestingly, spherical models outperformed some nonspherical models in terms of accuracy, which indicates the importance of proper shape characterizations if one wants to avoid such pitfalls of nonspherical models. They also showed that by considering simple particle characteristics (i.e., flatness and elongation) it is possible to obtain relatively accurate estimation of VA drag coefficient (average error of 8%).

Earlier quantitative shape analyses were limited to measurements of only a small number of particles [*Heiken*, 1972; *Bayhurst et al*., 1994; *Riley et al*., 2003; *Mills and Rose*, 2010], whereas recent instrumental developments allowed measurements of a high number (100,000 s) of projected and three-dimensional particle shapes [*Durant and Rose*, 2009; *Bagheri et al*., 2015; *Leibrandt and Le Pennec*, 2015; *Liu et al*., 2015]. Analyzing a high number of particle shapes as a function of size is necessary for deriving statistically robust shape parameters that help minimizing the uncertainties in transport and mass concentration calculations [*Bagheri et al*., 2015; *Liu et al*., 2015]. The higher the number of measured and analyzed particles, the smaller is the uncertainty of derived relevant shape descriptions such as the particle form or roundness.

Another parameter that controls the atmospheric lifetime and calculations of mass concentrations of VA particles is the mass density. The mass density is also needed to convert the particle volume to particle mass both in atmospheric measurements and in models. The mass density depends on the chemical composition

and on the vesicularity. The vesicularity is defined as the volume percent of internal void space in volcanic ash particles. Higher vesicularity results in lower densities. Thus, if vesicularity depends on particle size, the particle density varies with particle size as well. This is of importance for determining the terminal settling velocity and deposition patterns of ash particles [*Bonadonna and Phillips*, 2003; *Costa et al*., 2006]. Incorrect mass density assumptions also lead to errors in gravitational settling and dry deposition schemes in atmospheric models and to an overestimation or underestimation of mass concentration calculations in both model and measurements products. Typical mass density values are in the range of ρ = 2.35–2.45 g/cm^3 for glass shards, ρ = 2.70–3.30 g/cm^3 for crystals, and ρ = 2.60–3.20 g/cm^3 for lithic particles [*Wilson et al*., 2012; *Clarisse and Prata*, 2016].

1.3. Optical Properties

The most severe lack of information concerns the optical properties of VA particles. The optical properties are described by the complex refractive index,

$$N_\lambda = n_\lambda + i\, k_\lambda, \tag{1}$$

where n_λ is the real part, related to the refraction, and k_λ is the imaginary part related to the attenuation of incident light. The complex refractive index is therefore a quantitative measure of the particles' refraction properties, i.e., how they transmit, reflect, and absorb incident light, and is dependent on the chemical composition [*Ball et al*., 2015] of the material and on the particles' shape and density and hence can vary significantly.

Reliable information about the complex refractive index is necessary for ash remote sensing retrievals [*Krotkov et al*., 1997], optical ash measurement methods [*Bukowiecki et al*., 2011; *Tesche et al*., 2012], and also for quantifying weather and climate impacts of the ash [*Timmreck*, 2012; *Flanner et al*., 2014; *Vernier et al*., 2016] (see Figure 1). For example, the refractive index is a needed input parameter in radiative transfer models that are employed to simulate the backscattered top-of-the-atmosphere radiance to derive the aerosol optical depth and the effective particle radius of an ash cloud for remote sensing retrievals [*Krotkov et al*., 1999a; *Carn and Krotkov*, 2016].

Although the complex refractive index is known to be highly important for the detection and modeling of volcanic ash clouds, existing studies are limited. Different studies used different particle types such as volcanic ash particles, terrestrial rocks, and pure glasses [*Pollack et al*., 1973; *Volz*, 1973] to investigate either the complex refractive index or only the absorption part (k_λ) for either single wavelengths [*Ball et al*., 2015] or a broad wavelength range. Thereby, these studies used different theoretical and experimental approaches such as measurements of the diffused reflectance [*Patterson*, 1981; *Patterson et al*., 1983; *Krotkov et al*., 1999b; *Rocha-Lima et al*., 2014], direct transmittance [*Grainger et al*., 2013; *Ball et al*., 2015], a combination of both [*Pollack et al*., 1973], or calculations based on the chemical composition [*Kandler et al*., 2011]. In fact, many studies can be traced back to a single source of data [*Pollack et al*., 1973], which is based on the characterization of terrestrial rocks and glasses.

An overview about all available refractive index values for volcanic ash and glasses found in the literature is provided in Figure 2. The complex refractive index data are sorted by the igneous rock groups of the samples that are depending on the silica and total alkali contents ranging from basalt to rhyolite, and the wavelength. The overview also shows the main measurement systems operating in the relevant wavelength range.

The real part of the complex refractive index can be estimated by using different approaches such as the Becke line technique, where the particles are immersed in a matrix of resin or liquid with well-characterized optical properties, through reflectance measurements from bulk material or theoretical calculations. The total reflectance proportion is derived using the reflectance data directly or by using the information about the chemical composition of the samples. In the ultraviolet (UV) to near-infrared (NIR) wavelength range, typical values range between n_λ = 1.5 and 1.6 for silicate glasses and between n_λ = 1.45 and 1.65 for naturally occurring rocks and VA (depending on sample composition and wavelength) [*Pollack et al*., 1973; *Ball et al*., 2015].

The imaginary part of the complex refractive index can be retrieved either using both reflectance and transmittance data or based only on transmittance measurements. It can also be estimated from reflectance measurement only using the Kubelka-Munk theory, a phenomenological correlation between the total diffuse

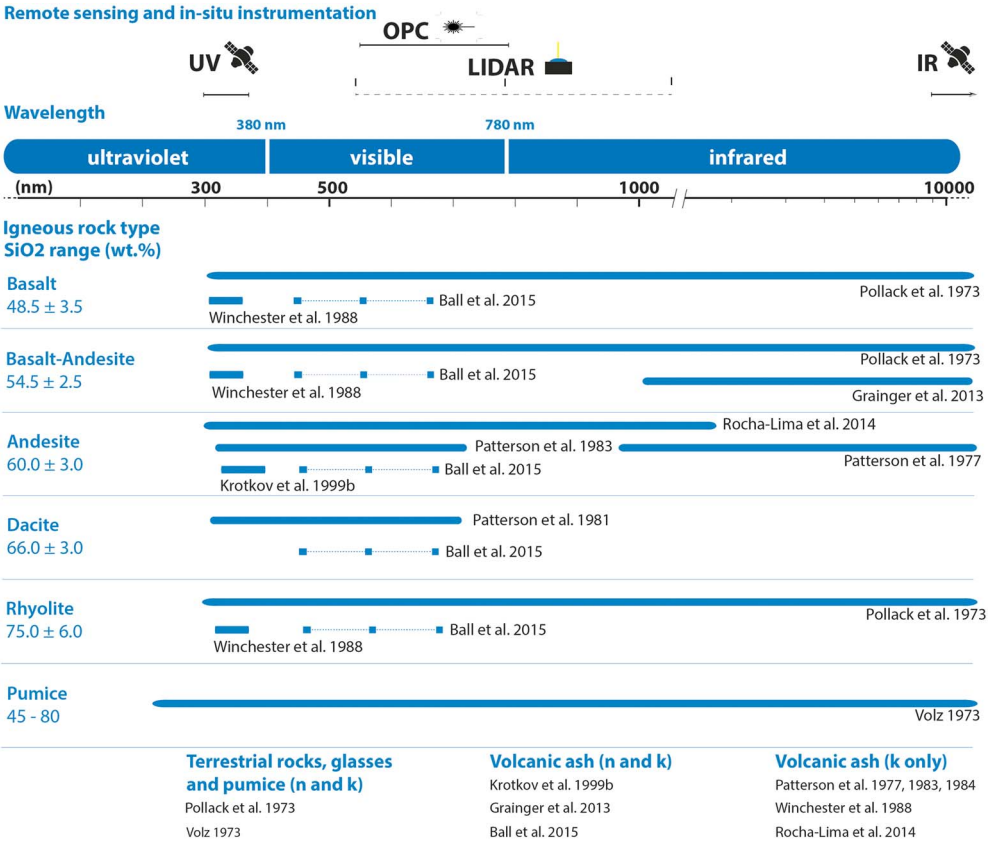

Figure 2. Overview of available refractive index values in the literature sorted by the main igneous rock types basalt to rhyolite (depending on silica content) including pumice and wavelength. On the top, we also marked the instruments operating in the corresponding wavelength ranges. These are optical particle counters (OPCs), light detection and ranging (lidar) instruments, and satellite retrievals operating in the ultraviolet (UV) and infrared (IR) range. Notice that some studies measured only the absorption properties, some both scattering (*n*) and absorption (*k*) properties, but only for single wavelengths, while others measured the properties for volcanic ask like material such as terrestrial rocks or glasses. The differences are indicated at the bottom of the figure.

reflectance of the sample and a concentration of bulk absorbing species using a scaling factor (absorption-to-scattering ratio of the material) as demonstrated by *Patterson* [1977, 1981]. This technique requires information about the size distribution and particle shape and relies on iterative procedures and complex forward modeling [*Nobbs*, 1985].

Direct transmittance measurements, however, allow determining the absorption properties of the ash samples directly, as soon as *k* is related to the portion of light that is absorbed, described by the Lambert-Beer law [*Zaccanti and Bruscaglioni*, 1988]. The samples can be either rock material with varying thicknesses (larger sample) [*Pollack et al*., 1973], particle powder embedded in a host matrix, or single particles immersed in liquid as demonstrated by *Ball et al*. [2015]. Furthermore, the absorption properties, other than the reflectance properties, can also be derived from satellite data [*Ishimoto et al*., 2016] directly, but these retrievals are subject to their own assumptions and limitations.

Earlier studies reported high variations in absorption values in the range of k_λ = 0.1 and 0.0001 [*Patterson*, 1981; *Patterson et al*., 1983], whereas later studies reported smaller variations with values in the range between k_λ = 0.001 and 0.00001 [*Krotkov et al*., 1999a; *Grainger et al*., 2013; *Rocha-Lima et al*., 2014; *Ball et al*., 2015]. Generally, basaltic ash samples with a low silica content (~48 wt % SiO_2) show the highest absorption, while rhyolitic ash samples with a high silica content (>70 wt % SiO_2) show the lowest absorption. For a more general characterization of the scattering and absorption characteristics of volcanic ash, it would be important to have an extensive set of measurements of n_λ and k_λ values for many different ash types as well as over the a wide wavelength range relevant for atmospheric measurements and modeling.

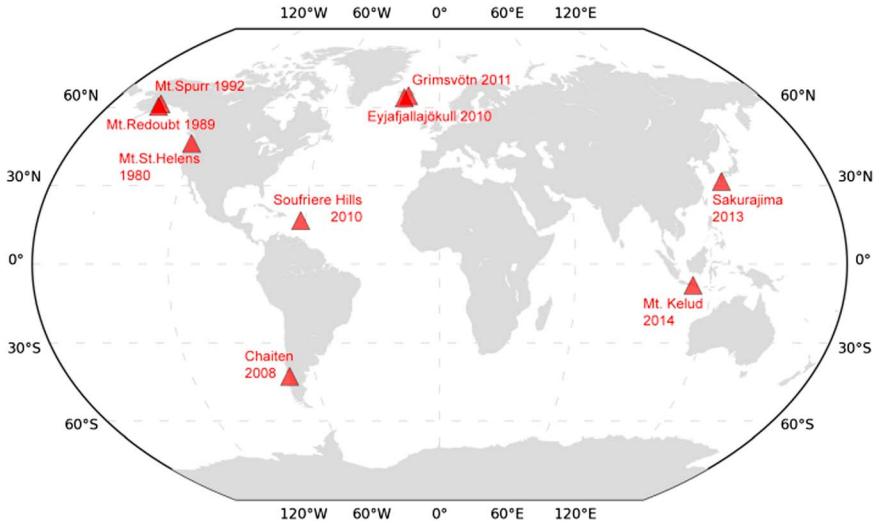

Figure 3. Geographical locations where volcanic ash samples of this study were collected. All ash samples represent proximal-medial to distal fallout and originate from volcanoes in North America (Mount Spurr 1992, Redoubt 1989, and Mount St. Helens 1980), South America (Chaitén 2008), the Caribbean Islands (Soufrière Hills 2010), Iceland (Grímsvötn 2011 and Eyjafjajökull 2010), and from the western Pacific region (Mount Kelud 2014 and Mount Sakurajima 2013).

1.4. Scope of This Study

To date, few studies exist that present measurements of both the physicochemical and optical properties of volcanic ash particles, and we are not aware of any other study that has made such measurements in a systematic way for ash particles originating from a large range of different eruptions from different volcanoes. In this study, we provide a data set for physical (particle size, morphology, and density), chemical (bulk and surface chemistry as well as glass contents), and optical properties (complex refractive indices in the UV-Vis-NIR range) of a representative selection of volcanic ash samples from nine different volcanic eruptions covering the full variability in silica content (50–80 wt % SiO_2). A user of our data set, who is interested in another eruption for which the magma type that produced the ash is known, will be able to select the physical and optical properties of our most representative ash samples and use these values for, e.g., satellite retrievals or model calculations for the eruption of interest. Our data set may thus serve as a reference for future studies requiring parameters describing VA properties. We captured the natural variability of ash physicochemical and optical characteristics through a combination of empirical analytical methods (e.g., image analysis, Archimedean densitometry, energy dispersive spectroscopy, X-ray photoelectron spectroscopy, light microscopy, and UV/Vis spectrophotometry) and theoretical calculations. This paper is structured as follows: In section 2 we introduce the methods we used, in sections 3 and 4 we present the results and discuss their implications and their context to existing studies, and in section 5 we present conclusions.

2. Methods

2.1. Sample Selection, Origin, and Sampling

For the investigation of the microphysical, chemical, and optical properties, we selected nine VA samples from different volcanoes and eruptions (Figure 3). The selection of the samples was based on (a) the wide range of silica contents (from basaltic to rhyolitic ash), (b) their origin from explosive (volcanic explosivity index $\leq$5) eruptions with a high content of fine ash particles (particle diameter, $d < 63$ μm), and (c) the fact that the selected eruptions had a large impact on the society (impact on infrastructures and aviation). Furthermore, the samples represent proximal-medial to distal fallout samples as well as one sample from a pyroclastic density current (PDC). Material from most of the samples was used in various studies before (see references in Table 1), but no study has made a comprehensive analysis of particle microphysical, chemical, and optical characteristics for the complete silica content range. Table 1 presents an overview of the different ash types, their chemical classification, and details about sample location and distance from the volcano sorted according to geographic location from North America to the western Pacific region.

Table 1. Overview of Volcanic Ash Samples Included in This Study Including Sample ID, Classification Into the Main Igneous Rock Types, Volcanic Explosively Index (VEI), and Information About Eruption Date, Sample Location, and Distance From the Volcano

Sample ID	Volcano	Eruption Date	VEI	Sample Location		Distance from Volcano [km]	References
				Lat.	Lon.		
GRI	Grimsvötn, Iceland	May 2011	4	63.78°N	18.09°W	80	–
KEL	Mount Kelud, Indonesia	February 2014	4	07.93°S	112.31°E	215	–
EYJ	Eyjafjallajökull, Iceland	April–June 2010	4	63.63°N	19.62°W	35	*Gislason et al.* [2011], *Gudmundsson et al.* [2012]
SPU	Mount Spurr, United States	September 1992	4	61.74°N	47.60°W	250	*McGimsey et al.* [2001], *Rose et al.* [2001], *Rose and Durant* [2009]
SAK	Mount Sakurajima, Japan	August 2013	–	31.59°N	130.67°E	10	*Bagheri et al.* [2016]
MSH	Mount St. Helens, United States	May 1980	5	46.25°N	122.18	6	*Adams et al.* [1996], *Rose and Durant* [2009]
SOU	Soufriere Hills, United Kingdom	February 2010	–	16.72°N	62.18°W	5	*Cole et al.* [2015]
RED	Mount Redoubt, United States	December 1989	3	62.54°N	150.24°W	265	*Bayhurst et al.* [1994], *Schneider and Rose* [1994]
CHA	Chaitén, Chile	May 2008	4	43.33°S	72.47°W	60	*Alfano et al.* [2011]

The Mount Spurr (SPU) ash sample from the 1992 eruption was collected ~250 km east of the eruption location by the United States Geological Survey (USGS) Alaska Volcano Observatory. The eruption plume reached, at a peak altitude, the stratosphere and traveled eastward with the prevailing winds [*Schneider et al*., 1995], where the fine fraction of the deposits was collected under 23 cm of snow on Barry Glacier (23.2 g in 0.0625 m^2) shortly after deposition [*McGimsey et al*., 2001; *Rose et al*., 2001; *Durant and Rose*, 2009]. The Mount Redoubt (RED) ashfall sample from the 15 December 1989 eruption was collected ~265 km NE of the volcano by the USGS in March 1990. The sample was taken from the lower tephra layer embedded in a 1.5 to 2 m thick snow cover at Dateli Lake [*Bayhurst et al*., 1994; *Schneider and Rose*, 1994]. It is possible that a commercial aircraft that had a failure on all four engines due to volcanic ash ingestion [*Casadevall*, 1994] passed through the same cloud on the date of the Mount Redoubt eruption. The Mount St. Helens (MSH) ashfall sample from the 18 May 1980 pyroclastic density current (PDC) was taken from the Pumice Plain ~6 km north of the 1980 crater. The sample was collected in August 1981 from a cliff exposure where the unit could be clearly identified. The fine ash fraction in this sample is mostly coignimbrite ash that was elutriated from the PDC, rose to tropopause heights by convection, and fell out distally [*Adams et al*., 1996; *Munoz et al*., 2004]. The Chaitén (CHA) ashfall sample from the May 2008 eruption was collected ~60 km SE from ashfall deposits with consistent thicknesses [*Alfano et al*., 2011] in January 2009. The Soufríere Hills volcano (SOU) ashfall sample from the February 2010 dome collapse pyroclastic density column was collected ~5 km NE of the eruption by the Montserrat Volcano Observatory. The eruption plume reached altitudes up to 15 km, where an umbrella cloud was formed and dispersed by SE winds [*Cole et al*., 2015]. The Eyjafjallajökull (EYJ) ashfall sample from the 2010 eruption was collected ~35 km SW of the volcano by the Institute for Earth Sciences of the University of Iceland. The sample was taken after the first phase of the eruption in April 2010 [*Gislason et al*., 2011; *Gudmundsson et al*., 2012]. The Grímsvötn (GRI) sample from the 2011 eruption was taken ~80 km SW of the volcano (near Skógar) by the Düsseldorf University of Applied Sciences. In this case, the sample was collected on a car surface in an open barn. The Kelud (KEL) sample from the 2014 eruption was sampled at ~215 km distance from the volcano by the Indonesia Centre for Volcanology and Geological Hazard Mitigation. The eruption plume rose up to the stratosphere and dispersed particles over long distances. The ashfall sample was collected from the ground in April 2014, approximately 6 weeks after the eruption in Yogyakarta. Finally, the Mount Sakurajima (SAK) ash sample is associated with a Vulcanian explosive eruption event on 3 August 2013. It was collected at ~10 km distance directly after the eruption event. The ash-rich eruption plume reached 2.3 km [*Bagheri et al*., 2016].

2.2. Sample Preparation

For the different analytical approaches in this study, we separated the samples into two different subgroups: (1) loose powder samples and (2) embedded particles in a host matrix. The sample groups are illustrated in Figure 4. For simplification, the two subgroups will be mentioned in the text as powder samples and pellet samples. Powder samples were used for the measurements of particle size and complex morphology (form

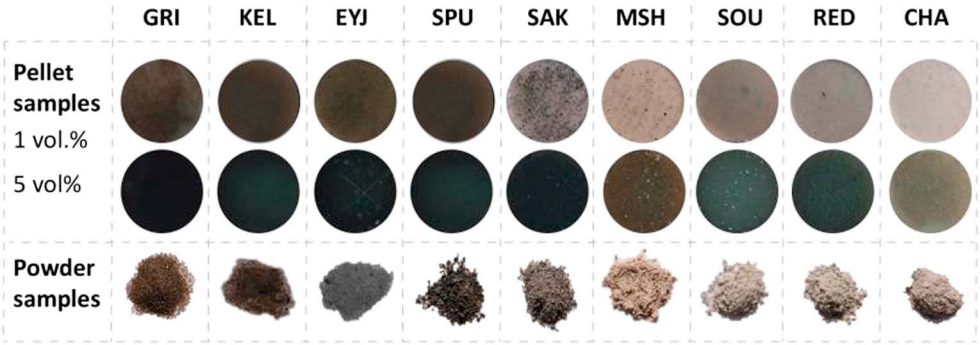

Figure 4. Overview about the two different sample subgroups. The top and middle rows show the 1 vol % and 5 vol % pellet samples, respectively, of the nine ash types.

and shape parameters), mass density, and the chemical composition of the particle surfaces. The particles were used without any additional treatment apart from a moderate sample drying (at 60°C) prior to each measurement. Pellet samples were used for the characterization of the bulk chemical composition and for the measurements of the optical properties. The pellets were prepared by embedding defined volume fractions (f) of ash particles in a clear polymeric host matrix (Struers Clarofast, hot mounting resin). We selected a resin that is transparent in the relevant wavelength range (λ = 300–1500 nm) and sufficiently conductive, stable under an electron beam and suitable for mechanical grinding and polishing. The mixture composed of ash and resin was subsequently pressed into a pellet using a hot embedding press (Struers LaboPress-3) under constant pressure (15 kN) and heating conditions (180°C). This approach ensures a porosity-free and compact embedded material for further analysis. The resulting pellet was then cut, grinded, and polished in several steps (final step was polishing with 2 μm diamond particle suspension) to produce a flat sample surface. After this process the samples were cleaned and dried in hot air. The final thickness t of these samples was t = 2–3 mm with a volume fraction of embedded volcanic ash particles between f = 0.01 and 0.05. Important to note is that this preparation procedure produced cross sections of the embedded particles near the pellet surface; therefore, the same samples were used for measuring both the bulk chemical composition and optical properties discussed in sections 3 and 4.

2.3. Chemical Characterization

The chemical characterization of VA provides key data for most of the measured and derived parameters in this study. The different ash samples were grouped, following a classification based on the total alkali (Na_2O and K_2O) and silica (SiO_2) content (so-called TAS classification) [*Le Bas and Streckeisen*, 1991], into the main igneous rock types basalt, basaltic-andesite, andesite, dacite, and rhyolite. In addition to the chemical composition of the bulk material, we also analyzed the chemical composition of the particle surface.

2.3.1. Bulk Material

For the measurement of the chemical composition of the bulk material, the embedded particles in the pellet sample were analyzed using field-emission gun scanning electron microscopy (FEG-SEM) with an integrated energy dispersive spectrometer (EDS). The FEG-SEM measurements were performed on a Nova NanoSEM650 microscope and the EDS analysis on an X-Max50 spectrometer. The samples were analyzed in high-vacuum mode and with a 20 kV accelerating voltage. A backscatter detector was used at a working distance of 8.1 mm. The SEM field of view was set to 300 μm × 300 μm to capture the microstructure and shape of embedded particles of sizes 1–100 μm. The sample elemental composition was recorded with an EDS micrometer-sized beam allowing determination of an average composition of the total cross-section area of the embedded particles. This approach gives representative results of all elements over the entire sample area and minimize measurement uncertainties. For each volcanic ash sample, the elemental compositions of several hundreds of particle cross sections (produced by the embedding and polishing process) were measured and processed. Major elements present in the composition of volcanic ash particles are Si, Al, Fe, Mg, Ca, Na, K, Ti, Mn, and O in varying concentrations. The elemental data of each component were first converted into weight percent of the corresponding oxides (oxide wt %) and subsequently averaged using a Gaussian

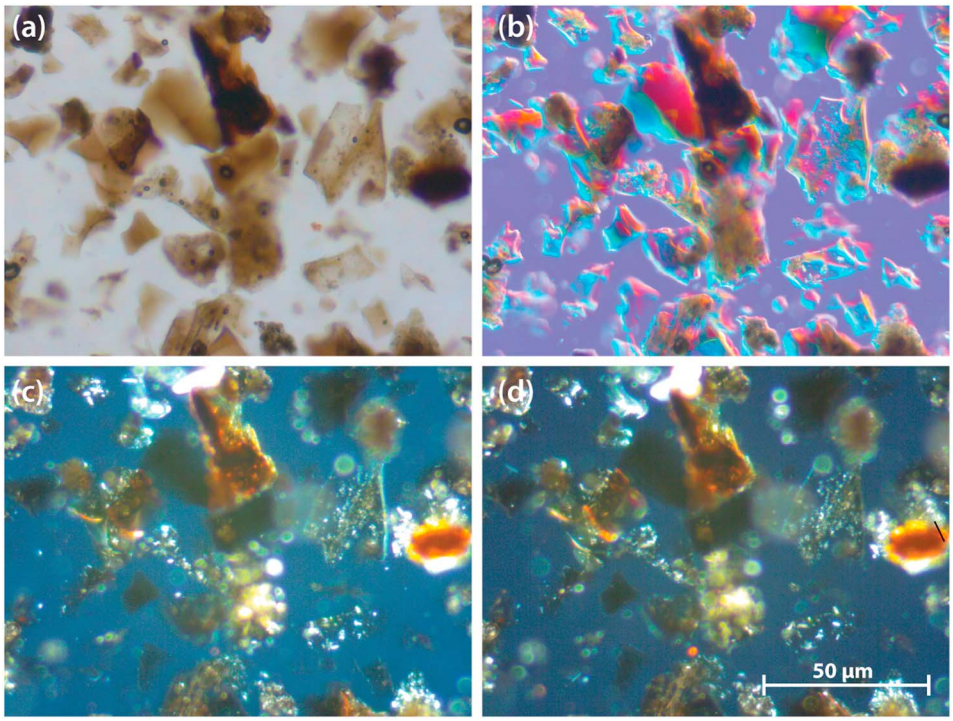

Figure 5. Optical microscope images of ash from the 2011 Grímsvötn eruption (sample GRI). (a) TL-BF: bright-field image, (b) TL-IC: interference contrast image, (c) TL-PL: cross-polarized image at 0°, and (d) TL-PL: cross-polarized image at 45°.

filter function (2-sigma ranges). The reported data do not account for the presence of water and are normalized (processing option: oxygen by stoichiometry).

2.3.2. Particle Surface

X-ray photoelectron spectroscopy (XPS) was used to measure the elemental composition and chemical state of the particle surfaces down to an average depth of 2–10 nm. The XPS analysis was carried out using a Kratos Axis Ultra^{DLD} spectrometer with a monochromatic Al Kα X-ray source (hv = 1486.7 eV). The spectra were acquired at a zero angle of emission using the hybrid analyzer mode (i.e., using both the electrostatic and magnetic lenses) at pass energies of 160 eV and 20 eV for the survey and high-resolution scans, respectively. The samples were placed in Cu-based stubs, and charge compensation was achieved by using a flood gun producing coaxial low-energy electrons, which resided on the sample surface providing charge neutralization. During the XPS analysis, the vacuum of the standard analysis chamber was set to 8×10^{-10} hPa. The measured spectra were energy corrected using the C1s peak for adventitious carbon (285 eV). For peak fitting we used linear and Shirley background types and for the quantification high-resolution peaks and Wagner sensitivity factors. The area of analysis was 700 µm × 300 µm and included several thousand particles. The averaged elemental composition were converted, like the EDs data, into weight percent of the corresponding oxides (oxide wt %).

2.3.3. Glass Contents

The measurements of glass and crystalline component phases within the selected ash samples were performed on a Leica Reichert Polyvar2 optical microscope equipped with light polarization and image capture software (Leica IM 500). The powder samples were mounted on a microscope glass sample holder using Crystalbond 509. We employed three modes of operation: (1) transmitted light (TL) bright-field (BF) illumination, (2) TL cross-polarized (PL) illumination at two different angles at 0° and 45° (two images) using polarized light, and (3) TL interference contrast (IC) illumination [*McCrone et al*., 1978].

Figure 5 shows an overview of images of the three modes for the example sample GRI. The TL-IC image (Figure 15b) was used to determine the total pixel area of the particles, after removing the background by an image processing procedure, whereas the TL-PL images were used to determine the total pixel area of component phases within the samples. It was then possible to calculate the total glass (amorphous)

fraction by analyzing these two areas. TL-BF images were used to correct for the presence of opaque particles, where no discrimination between the glass and crystal phases was possible.

2.4. Microphysical Characterization

2.4.1. Image Analysis of Particle Size and Morphology

For the measurement of particle size and morphometric characterization, we used an automated static particle imaging (ASPI) instrument (Malvern Instrument Morphologi G3). The ASPI is an optical analyzer for the characterization of the particle morphology on a two-dimensional projection area. A full description of the instrument and all relevant features can be found in *Leibrandt and Le Pennec* [2015] and *Liu et al*. [2015]. The ASPI instrument is a state-of-the-art instrument, which provides reliable and reproducible particle information for a statistically significant number of particles with a low relative standard deviation on average values (<0.2%) [*Leibrandt and Le Pennec*, 2015]. Therefore, the data acquired with this instrument can be used for a parameterization of different shape descriptions in particle transport and dispersion as well as climate models (Figure 1).

For the instrumental setup, we used the standard operation procedure described by *Leibrandt and Le Pennec* [2015] for two different microscope objective lenses. A 20X magnification objective lens was used for the particle sizes between 1.8 and 100 μm and a 5X magnification objective lens for the size range of 6.5–420 μm. The use of the 20X magnification objective was important as the 5X objective has a poorer resolution below 63 μm particles [*Leibrandt and Le Pennec*, 2015]. The particle sample area was set to 314.16 mm^2 for the 20X objective and 1256.64 mm^2 for the 5X objective to capture a high number of particles. The difference between the two sample areas guaranteed the characterization of a statistically adequate number of the less abundant larger particles. The total number of individual particles measured for each ash sample was between 10^6 and 10^7 based on an initial sample volume of 7 mm^3, providing high statistical significance. The light source was set to be diascopic, which means that the light shone from below the carrier unit to produce a sharp contrast between the dark ash particles and the light illuminated background. Due to the very narrow depth of field of the individual objective lenses, we used a two layer *Z*-stacking option. *Z* stacking is a function that takes several images, each at different heights *Z*, before these pictures are overlaid to form a single composite picture. This option ensures accurate focusing and a quasi-three-dimensional representation of the particle projection area.

The particle area is defined as the sum of individual pixels (a_p) ($A = \sum a_p$) within the borders of the detected area that is set by the threshold settings of the different objective lenses. The border represents also the particle perimeter (*P*) that is calculated using the Cauchy-Crofton equation ($P = \frac{\pi}{N} \sum_a^{\pi} I_\alpha d_L$), from the number of intercepts (*I*), formed by a series of parallel lines, with spacing d_L, exploring *N* directions, from α to π. Within this detected area, the distances (longest, intermediate, and shortest) of each particle axis can be directly measured. The particle length is defined as the maximum distance between two points on the perimeter parallel to the major axis, which is the angle of the major axis from a horizontal line. The particle width is defined as the maximum distance parallel to the minor axis, which passes through the center of mass at right angles to the major axis. The intermediate particle length is defined as the maximum distance between points on the particle axis with 45° inclination to the major axes. Illustrations of the particle area, the different distances, and the particle perimeter that are essential for further particle size, form and shape descriptions, are illustrated in Figure 6.

For the description of the particle size, we used the circle equivalent particle diameter ($d_{2\text{-D}}$), also known as the Heywood diameter, that relates the measured two-dimensional particle area to a particle size by the assumption that the measured particle has the same two-dimensional projected area as a circle

$$d_{2D} = \sqrt{4A/\pi}. \tag{2}$$

To describe particle form and shape, we chose three different nonsphericity parameters: the aspect ratio (AR), the Cox circularity (ϕ), and the Wilson shape parameter (WSP) introduced by *Wilson and Huang* [1979]. The AR is defined as the ratio between the longest distances of each major axis of the projected particle area

$$\mathrm{AR} = \frac{d_{I\_\mathrm{axis1}}}{d_{I\_\mathrm{axis2}}} \tag{3}$$

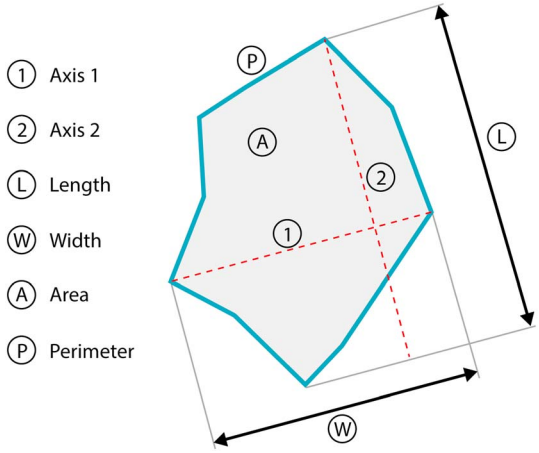

Figure 6. Illustration of the measured size and shape parameters by the ASPI and the DIA instruments. The dashed lines indicate the main particle axis in each direction.

and is a classical description of the particle elongation. The AR, for example, is employed in radiative transfer models when nonsphericity of the ash particles is considered [*Kylling et al*., 2014] or as one of the shape descriptors for estimating drag coefficients of nonspherical particles [*Bagheri and Bonadonna*, 2016b]. The true particle sphericity is a three-dimensional characteristics of particle shape, which is defined as the ratio of surface area of a sphere with the same volume as the particle to the surface area of the particle [*Wadell*, 1932]. For irregular particles, however, the surface area is not an absolute value and depends on the scales at which the measurements are carried out [*Bagheri et al*., 2015]. *Bagheri et al*. [2015] showed that a two-dimensional surrogate for the true sphericity of VA and lapilli-size particles (measured with resolutions of 1–100 μm) are the circularity measures. Here we measured the Cox circularity (φ) [*Cox*, 1927] that is found to have a high correlation with sphericity of VA with vesicular surfaces (opening diameter of the vesicles on the surface is 5–40% of particle diameter, see *Bagheri et al*. [2015] for more details). Parameter ϕ is defined as the ratio of the circle equivalent particle two-dimensional projected area to the surface area represented by the square of the particle perimeter

$$\phi = \frac{4\pi A}{P^2}. \tag{4}$$

The last parameter is the Wilson shape parameter (WSP) [*Wilson and Huang*, 1979]. The WSP is defined as the ratio of the sum of the intermediate (d_{l_axis3}) and shortest (d_{l_axis2}) distance to the longest (d_{l_axis1}) axis

$$\mathrm{WSP} = \frac{d_{l\_axis3} + d_{l\_axis2}}{2\, d_{l\_axis1}}, \tag{5}$$

and is often used in radiative transfer models. All described shape parameters are normalized and range from 0 to 1, where 1 corresponds to a perfectly spherical particle. For a validation of the measured size and shape parameter by the ASPI instrument, we used a second instrument (CamsizerXT). This instrument, a dynamic image analyzer (DIA), uses the same physical approach, but in a wet dispersion module configuration, where the particles are suspended in water and circulated through the measurement chamber (two cameras setup) [*Retsch Technology GmbH*, 2016]. The use of a second instrument allowed us to identify and eliminate potential instrumental biases.

2.4.2. Dense-Rock Equivalent Mass Density

We used two different approaches to determine the mass density: (1) direct measurements of the dense-rock equivalent (DRE) mass density of the particle skeleton using Archimedean densitometry and (2) theoretical mass density calculations based on mass fractions for the major oxides as obtained from the compositional analysis and crystalline volume data from *Lange and Carmichael* [1987]. The mass density measurements were done using a pycnometer (also called specific gravity bottle), which involved weighing the ash sample in air (m_s) and in another fluid (m_l) (here water at constant and known temperature) with a well known density (ρ_l). The measured mass density is derived from the following equation

$$\rho_m = \frac{m_s}{V_c - (m_l/\rho_l)}, \tag{6}$$

using the mass of the particle sample (m_s) and the difference between the total volume of the cylinder (V_c) and the water volume ($V_l = (m_l/\rho_l)$). Every ash sample was analyzed several times (including measurements at different water temperatures) to ensure reproducible and reliable results. This approach is accurate, elaborative, and well known for measuring the mass density of solid materials over a large range of particle sizes (fine ash fraction) [e.g., *Pistolesi et al.*, 2014].

The second method to determine the mass density of the samples is to relate the chemical composition of the bulk ash material directly to its mass density. This approach allows a consistency check of the measured mass density values and can be used to calculate the mass density when no densitometry measurements are possible or only chemical compositional data are available. For the theoretical mass density

$$\rho_t = \frac{\sum_{i=1}^{n} M_i\, X_i}{\sum_{i=1}^{n} \overline{V_i} X_i} \tag{7}$$

we used EDS data and the component specific volume, where the sum of the partial molar mass of each component (M_i) and the component mole fractions (X_i) is divided by sum of the partial volume of each oxide component ($\overline{V_i}$) and the component mole fractions (n being the total number of major components within the sample). The partial volumes of each oxide component are based on solid particles and were taken from *Lange and Carmichael* [1987].

2.5. Optical Characterization

The complex refractive index (RI) is a complex number and a quantitative measure of the reflectance, transmittance and absorption properties of a substance. Reliable information about the RI is important to relate optical measurement signals to particle information such as size (effective radius), size distribution, and ultimately the ash mass concentration. It is also needed in radiative transfer models for a quantification of the impact of volcanic ash on the Earth's radiative budget. The RI (N) is a function of the light wavelength (λ) and the chemical composition of the sample (see equation (1)).

The amount of direct and diffused refraction and attenuation of incident light by the different samples was measured using a commercial double-beam UV/Vis/NIR spectrophotometer (Perkin Elmer Lambda 950) equipped with a white Ulbricht integrating sphere. The integrating sphere was Spectralon covered to accomplish the diffuse signal detection. The instrument was equipped with sample thickness compensating detector optics and had a measurement range of λ = 250–2500 nm. The analysis spot on the sample surface was set to 10 mm × 5 mm, which allowed representative surface integration of the signal. The instrument has two light sources: a deuterium lamp for the UV range (up to 400 nm) and a tungsten lamp for the rest of the spectrum (Vis/NIR). The slit widths were set for 2 nm spectral resolution.

Measurements of light through fine-grained particles embedded in a host material (pellet sample) is a direct method that enabled us to determine k_λ in a wide spectral range. Reliable transmission measurements for our samples could be made in the wavelength range between λ = 300 and 1500 nm due to presence of specific absorption bands of the used resin for $\lambda > 1500$ nm. The volume averaged imaginary part of the refractive index (k_λ) of the ash samples can be calculated using Beer's law

$$I_{(\lambda)} = I_{0(\lambda)} e^{-\alpha_{\mathrm{abs}(\lambda)} t}, \tag{8}$$

where $I_{0(\lambda)}$, $I_{(\lambda)}$, $\alpha_{\mathrm{abs}(\lambda)}$, and t are the intensity measured in absence of the sample, the measured intensity of the sample (ash samples in host material), the volume absorption coefficient, and the sample thickness respectively. The volume absorption coefficient

$$a_{(\lambda)} = \frac{4\pi k_{\mathrm{eff}(\lambda)}}{\lambda}, \tag{9}$$

is related to λ and the effective extinction coefficient part ($k_{\mathrm{eff}(\lambda)}$) of the complex refractive index. By combining equations (8) and (9), we can calculate $k_{\mathrm{eff}(\lambda)}$ for the pellet sample (ash samples in host material):

$$k_{\mathrm{eff}(\lambda)} = \frac{\lambda}{4\pi t}\left(-\ln\left(\frac{I_{(\lambda)}}{I_{0(\lambda)}}\right)\right), \tag{10}$$

As a final step, the material specific extinction coefficient ($k_{\mathrm{ash}_{(\lambda)}}$) for the pure ash sample can be calculated by dividing $k_{\mathrm{eff}(\lambda)}$ by the volume fraction of the embedded ash in the host material ($f = V_T/V_{\mathrm{ash}}$)

$$k_{\mathrm{ash}(\lambda)} = \frac{k_{\mathrm{eff}(\lambda)}}{f}. \tag{11}$$

The transmittance measurements were conducted for two different volume fractions ($f = 0.01$ and 0.05) to avoid potential biases due to the particle amount in the pellet sample. The volume fractions were calculated using the measured mass density values of the samples and the weighed ash particle mass. Results for the two volume fractions were subsequently averaged and the deviation taken as a measure of the uncertainty of the imaginary part determination. To remove the host material contribution at specific wavelengths, we applied a second-order polynomial.

To obtain n_λ, we used a model that is a combination of Sellmeier dispersion equations [*Weber*, 2003] in combination with a theoretical calculation of the refractive index from chemical composition data as described by *Church and Johnson* [1980]. This approximate approach has been caused by the fact that the total integrated reflection values of our samples embedded in the host matrix (pellet samples), also measured by the spectrophotometer, resulted in much higher reflectance values (30–40%) than conceivable considering the chemical and morphological nature of the powders. Potential reasons for such high reflectance are not entirely investigated, but part of ongoing research. Simultaneous elaboration of reflectance and transmittance data will bring most reliable empirical data on the RI of the ashes.

The model is based on dispersion curves for known chemical compositions and theoretical calculations of the refractive index. The Sellmeier equation is a semiempirical relationship between refractive index and wavelength for a transparent to slightly absorbing medium (in condition $k \ll n$). The form of the Sellmeier equation is

$$n_\lambda^2 = 1 + \Sigma\left[\frac{B_i\lambda^2}{\lambda^2 - C_i}\right], \tag{12}$$

where the n is a function of the light wavelength (λ) and two empirically determined Sellmeier coefficients B and C. These dimensionless coefficients are material specific and represent an absorption of strength B_i at a wavelength $\sqrt{C_i}$. We applied the Sellmeier equation to all oxide components found in the ash particles multiplied by the weight fractions (w_i) of the major oxides, derived from the EDS bulk-compositional data, to obtain an averaged dispersion function. This calculation gives the weighted dispersion of the scattering part as a function of wavelength in the range between 300 and 1500 nm. To derive the material specific n_m, the calculated dispersion curve was fitted using single point values for a defined chemical composition and a single wavelength (in the visible range). The single point calculation

$$(n_m - 1) = \Sigma_{i=1}^{n_m} x_i w_i \tag{13}$$

is based on an arc-function, a quantitative relationship between the chemical composition of the sample and refractive index of individual components, where w_i is multiplied by empirically derived refractivity material specific constants (x_i) for major component oxides. The individual constants are obtained by the Becke line method of pure components and are taken from *Church and Johnson* [1980].

Table 2. Normalized Averaged Bulk-Chemical Composition of Ash Samples in wt % Measured by EDS, Including Composed Alkali Oxides and Calculated Ratios Between Individual Elements and the Predominate SiO_2 Content[a]

	GRI	KEL	SAK	EYJ	SPU	RED	SOU	MSH	CHA
				Major oxides ($\mu \pm \sigma$)					
SiO_2	51.7 ± 0.7	56.1 ± 7.6	60.0 ± 7.7	61.2 ± 3.8	61.7 ± 3.4	69.4 ± 8.7	68.4 ± 9.3	68.6 ± 7.1	77.1 ± 1.2
Al_2O_3	13.6 ± 0.6	19.2 ± 12.2	18.3 ± 10.6	14.7 ± 4.0	19.0 ± 4.7	16.9 ± 6.4	15.9 ± 7.4	17.1 ± 4.5	13.1 ± 0.8
FeO	13.3 ± 0.7	4.89 ± 5.5	5.70 ± 7.6	8.25 ± 3.6	4.54 ± 2.5	2.12 ± 3.1	2.83 ± 4.8	2.67 ± 5.6	1.12 ± 0.4
MgO	5.83 ± 0.5	5.33 ± 8.1	4.10 ± 7.4	2.13 ± 2.3	2.04 ± 2.7	1.29 ± 4.8	2.71 ± 6.5	0.82 ± 3.2	0.00 ± 0.0
Cao	9.54 ± 0.4	11.6 ± 6.3	7.41 ± 4.9	4.92 ± 2.4	6.48 ± 2.4	4.08 ± 3.7	4.61 ± 3.2	3.58 ± 2.7	1.27 ± 0.3
Na_2O	3.01 ± 0.4	2.26 ± 1.6	3.27 ± 2.0	5.26 ± 2.1	4.45 ± 1.0	4.39 ± 1.2	4.10 ± 1.6	5.30 ± 1.6	4.38 ± 0.5
K_2O	0.15 ± 0.3	0.41 ± 0.9	0.76 ± 1.1	1.66 ± 0.9	1.29 ± 1.0	2.11 ± 1.3	1.31 ± 1.2	1.76 ± 1.3	2.94 ± 0.3
TiO_2	2.70 ± 0.3	0.18 ± 0.3	0.16 ± 0.5	1.75 ± 2.5	0.42 ± 0.8	0.05 ± 0.2	0.02 ± 0.1	0.17 ± 1.1	0.04 ± 0.3
MnO	0.00 ± 0.0	0.14 ± 0.3	0.07 ± 0.2	0.00 ± 0.0	0.00 ± 0.0	0.04 ± 0.2	0.03 ± 0.2	0.00 ± 0.0	0.00 ± 0.0
Total	99.8	100	99.7	99.8	100	100	99.9	100	100
Alkali ($Na_2O^+ K_2O$)	3.16 ± 0.6	2.67 ± 2.2	4.04 ± 2.4	6.92 ± 2.6	5.74 ± 1.3	6.50 ± 1.8	541 ± 2.0	7.06 ± 2.2	7.31 ± 0.6
				Ratios					
Al_2O_3/SiO_2	0.26	0.34	0.30	0.24	0.31	0.24	0.23	0.25	0.17
FeO/SiO_2	0.26	0.09	0.09	0.13	0.07	0.03	0.04	0.04	0.01
MgO/SiO_2	0.11	0.10	0.07	0.03	0.03	0.02	0.04	0.01	0.00
Cao/SiO_2	0.18	0.21	0.12	0.08	0.10	0.06	0.07	0.05	0.02
Na_2O/SiO_2	0.06	0.04	0.05	0.09	0.07	0.06	0.06	0.08	0.06
K_2O/SiO_2	0.00	0.01	0.01	0.03	0.02	0.03	0.02	0.03	0.04
TiO_2/SiO_2	0.05	0.00	0.00	0.03	0.01	0.00	0.00	0.00	0.00
MnO/SiO_2	0.00	0.00	0.00	0.00	0.00	0.00	0.00	0.00	0.00
$Alkali/SiO_2$	0.06	0.05	0.07	0.11	0.09	0.09	0.08	0.10	0.09
				Componentry (% ± σ)					
Glass phase	50.9 ±1.8	50.7 ±3.1	60.6 ±2.3	54.2 ±8.0	57.6 ±6.5	69.5 ±7.1	65.3 ±2.4	69.5 ±3.0	72.0 ±1.7
Crystalline phase	49.1	49.3	39.4	45.8	42.4	30.5	34.7	30.5	28.0
Ash type	Basalt	Basalt-andesite	Andesite	Trachy-andesite	Andesite	Dacite	Dacite	Dacite	Rhyolite

[a]The samples were ordered according to their SiO_2 and total alkali contents into the main igneous rock classes indicated in the table.

3. Results

3.1. Chemical Composition

Table 2 shows the averaged chemical composition in oxide weight percent for all nine volcanic ash samples. The VA samples show characteristic compositions over a large SiO_2 and total alkali (TA) content range (51.7 to 77.1 wt % and 2.67 to 7.31 wt %, respectively). The mafic basaltic (GRI) and the felsic rhyolitic (CHA) ash samples show only small variations in composition, represented by their standard deviation, both in TA (±0.43% and ±0.64%) and in SiO_2 (±0.73% and ±1.19%) content, whereas the basaltic-andesitic to dacitic (intermediate volcanic rock range) samples show greater compositional variations and span over more than one rock type group (Figure 7). However, all samples could be classified into one defined igneous rock group as indicated by the colors in Figure 7. For further analysis (mass density and optical properties), we averaged the samples SPU, SAK, and EYJ for the andesitic ash type and MSH, SOU, and RED for the dacitic ash type. In none of the samples we found a size dependent chemical composition variation (largest analyzed particle size was 100 μm), but some individual particles showed very different SiO_2 content (<5% of all particles) due to the glassy phase fraction within the samples.

Figure 8 shows the variation of the different oxides in the bulk composition with varying SiO_2 contents. FeO is decreasing with increasing SiO_2 in accordance with the expected variations of Fe contents in the magmas. Fe contents tend to decrease with increasing SiO_2, from 7–8 wt % in basaltic magmas to ~2 wt % in rhyolitic magmas [*Le Maitre*, 1976; *Rogers and Hawkesworth*, 2000]. CaO and MgO follow the same trend as FeO (r^2 values between 0.5 and 0.85), which indicates that FeO, CaO, and MgO exist mostly in the silicate phase where Fe^{2+}, Ca^{2+}, and Mg^{2+} occupy interstitial sites between the silicate tetrahedral [*Mysen and Richet*, 2005]. The alkali oxides K_2O and Na_2O increase with increasing SiO_2 indicative of their participation in the SiO_2 glassy phase (Figures 9 and 10). Al_2O_3 present in alumino-silicates should increase with SiO_2 if SiO_2 was exclusively associated with alumino-silicates. However, the crystalline SiO_2 content also increases with increasing SiO_2 wt % in andesitic, dacitic, and rhyolitic compositions. The presence of Al_2O_3 in the same phase with SiO_2, but also as an independent phase, may explain why Al_2O_3 does not show a clear trend (ratios between 0.24 and 0.31, except for CHA sample due to very high SiO_2 content). TiO_2 shows the same trend as

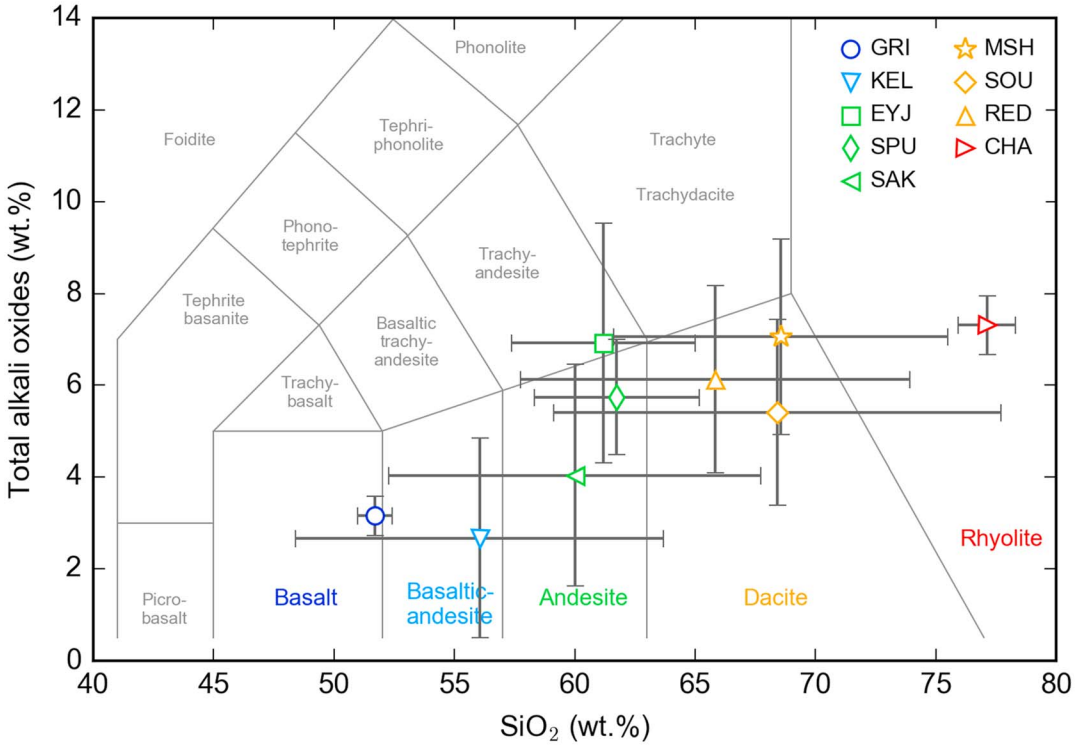

Figure 7. Classification of ash samples following their mean total alkali and silica (TAS) contents based on energy dispersive spectroscopy (EDS) data into the main igneous rock types. The colors in the plot represent the main igneous rock groups for basaltic (dark blue), basaltic-andesitic (blue), andesitic (green), dacitic (orange), and rhyolitic (red) ash types, that are used for the presentation of the complex refractive index data in section 3.2.

FeO, as TiO_2 has a stronger presence in lower silicate magma compositions. The calculated ratios between the individual components and SiO_2 are also summarized in Table 2. The measured chemical compositions of the ash samples correspond well with values reported in the literature (see references in Table 1).

3.2. Glass Contents

The correlation between the measured SiO_2 contents (bulk SiO_2 from EDS measurements) and the analyzed glass contents (analyzed light microscopy images) is shown in Figure 10. The colors represent the igneous rock types following Figure 6. We found that the mean glass contents of the ash samples ranged between 50% (2-D cross-sectional area analysis) glass content for the basalt/basaltic-andesite samples (GRI and KEL)

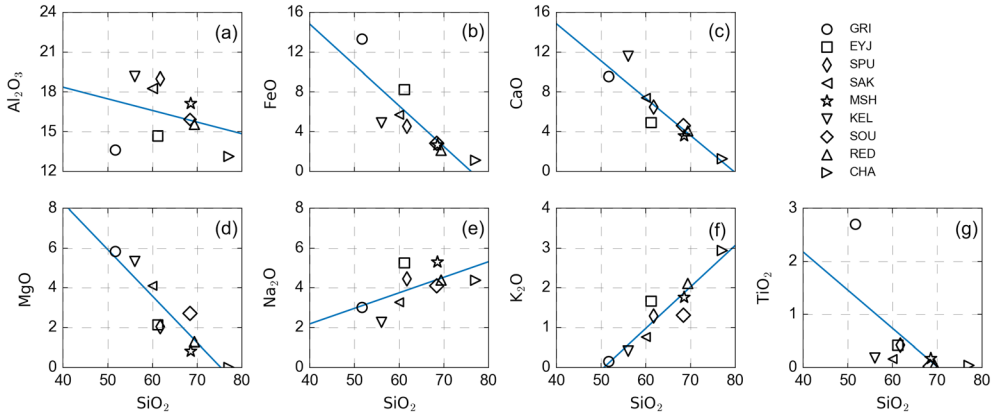

Figure 8. Correlation of the main chemical components with the silica content for the bulk-composition. These are (a) Al_2O_3/SiO_2 ratio, (b) FeO/SiO_2 ratio, (c) CaO/SiO_2 ratio, (d) MgO/SiO_2 ratio, (e) Na_2O/SiO_2 ratio, (f) K_2O/SiO_2 ratio, and (f) TiO_2/SiO_2 ratio. The blue lines indicate the resulting regression functions between each component.

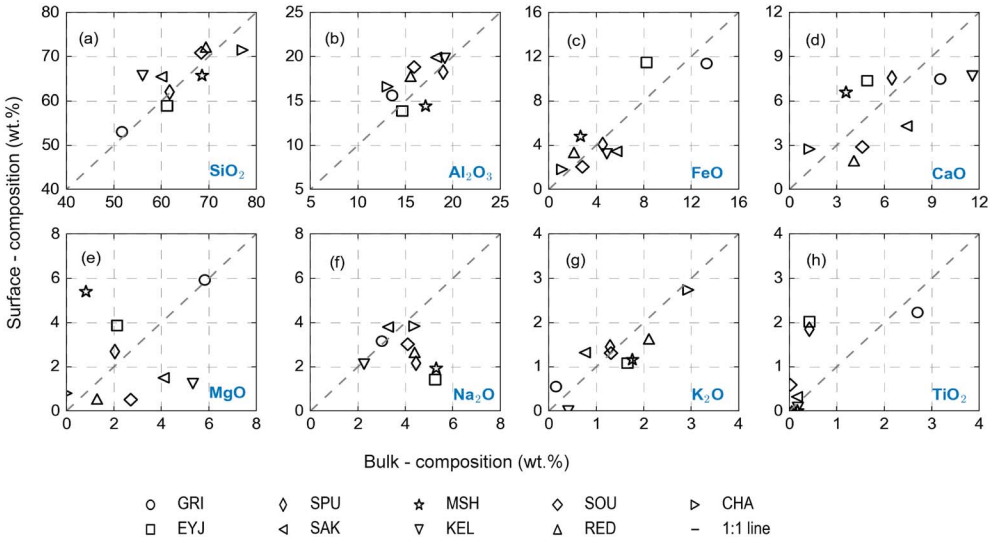

Figure 9. Correlation of the surface-composition (*y* axis) and the bulk chemical compositions (*x* axis). The dashed lines indicate the 1:1 line corresponding to an identical composition of the particle bulk and the particle surface. The different panels show correlations for (a) SiO_2, (b) Al_2O_3, (c) FeO, (d) CaO, (e) MgO, (f) Na_2O, (g) K_2O, and (f) TiO_2.

and 72% glass content for the rhyolitic sample (CHA). However, the variation within each sample represented by the error bars indicates that individual particles can have smaller or higher values. Furthermore, we found that within individual compositional classification types the glass contents can vary up to 20% (Table 1).

3.3. Particle Size Distribution

The box-whisker plots of the particle number distributions of the ash samples are shown in Figure 11. The mean and median particle sizes, indicated by the red line and diamonds, respectively, vary from sample to sample (depending on distance between the eruption and sample location, eruption style, and meteorological conditions), but all ash samples show a comparable number distribution with a median size between 2.4 μm for GRI and 11 μm for KEL. The minimum detected particle diameter of each sample is 1.5 μm, due to the lower particle size threshold of the instrumental setting, whereas the maximum particle diameters are greater than 100 μm. The maximum particle sizes vary between 120 μm for SPU and 280 μm for SAK but represent less than 1% of the total number distribution indicated by the blue crosses.

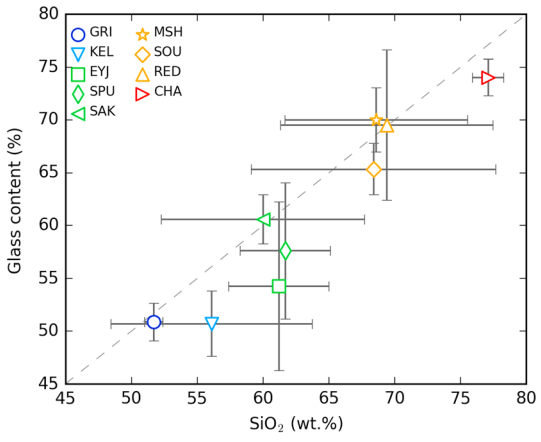

Figure 10. Comparison of SiO_2 contents (wt %) and glass contents (%) for the nine ash samples. The colors indicate the igneous rock types according to the classification in Figure 7. SiO_2 data are based on bulk composition measurements (EDS) and the glass content data on light microscope image analysis.

Additional sensitivity tests with a 50X objective lens indicate that the minimum particle size in each sample is smaller (<1 μm), but the mean and median size of the particle size distribution changed only marginally. The majority of all particles (25–75% range) in each sample range between 2 μm for GRI and 20 μm for KEL (indicated by the boxes) and are therefore within the particle size range that is most relevant for atmospheric long-range transport.

3.4. Particle Morphology

Particle morphological parameters within the measured ash samples displayed a wide range of variability, which decreased as particle size increased (Figure 13, blue markers).

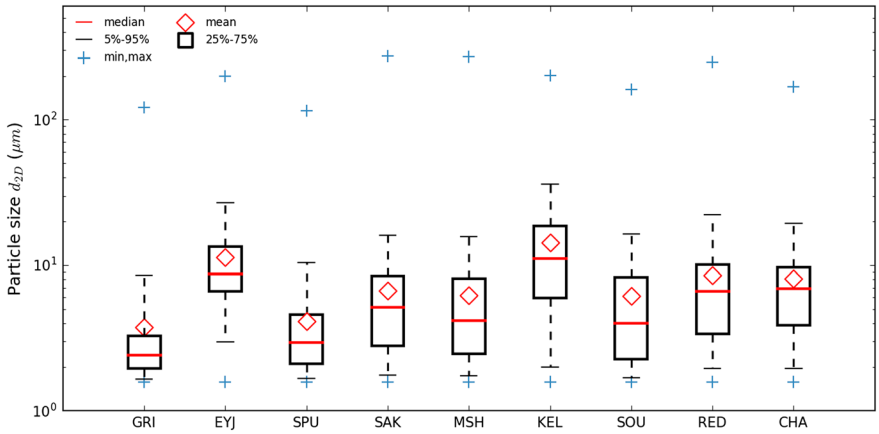

Figure 11. The box-whisker plot of the particle number distribution of each sample measured by ASPI. The red solid line indicates the particle median diameter, the diamond marker the mean diameter, the boxes the particle fraction within the 25–75% quartiles of the median, the dashed lines the 5–95% quantiles, and the red crosses the minimum and maximum detected circle equivalent particle diameters ($d_{2\text{-D}}$).

Particle morphology was characterized in coarse ($d_{2\text{-D}}$ = 63–100 μm) and fine ($d_{2\text{-D}} < 63$ μm) fractions for each ash sample (Figure 12). For a consistency check, we also evaluated the differences between the <20 μm size range (very fine ash fraction) and the fraction between 20 and 63 μm. As we found no significant differences between these two size fractions, we report values only for the fine and coarse ash fractions.

Figure 12 shows the three shape parameters for all samples separated into the fine and coarse ash fractions measured by ASPI. One the one hand, the shape parameter mean values are remarkably consistent between the nine different ash samples, with only 2.35–6.25% variation for the fine fraction and 5.32–13.2% variation for the coarse ash fraction.

On the other hand, the variability of particle shapes within each ash sample, indicated by the standard deviation, is much higher (up to 20%) as the shapes for individual particles can range from spherical to highly nonspherical (see blue dots in Figure 13). The aspect ratio and the Wilson shape parameter, which both describe the particle elongation [*Bagheri et al.*, 2015], indicate very small differences between the fine and the coarse mode particles, whereas the Cox circularity is larger for smaller particles.

In addition to the comparison of the averaged shape parameters for the coarse and fine fraction of the ash samples, we also analyzed the shape directly as a function of particle size in the size range <100 μm (Figure 14). Since there were relatively small differences in the shape parameters between the different ash samples, we only show the size-dependent shape parameter for all samples together. Therefore, each line

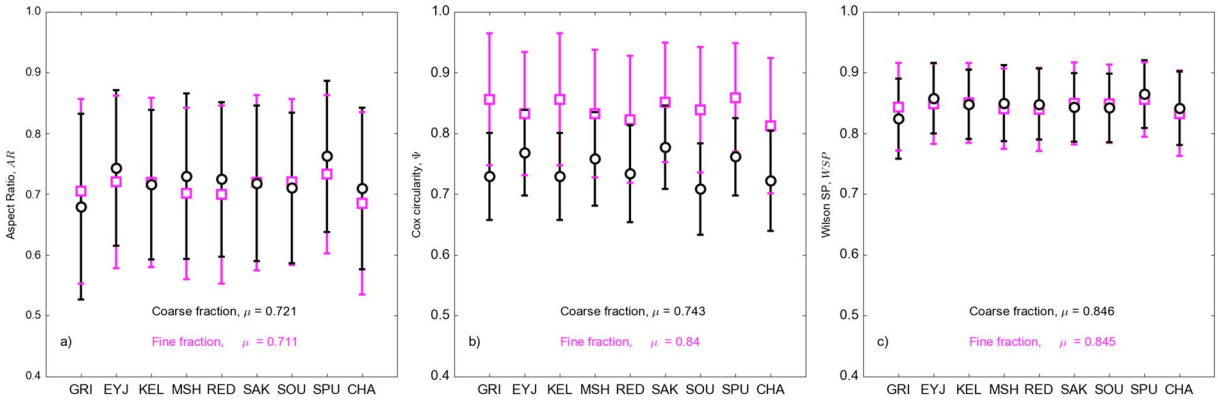

Figure 12. (a) Aspect ratio, (b) particle Cox circularity, and the (c) Wilson shape parameter measured by ASPI for the nine different ash samples. The black and gray lines indicate the coarse ($d_{2\text{-D}}$ = 63–100 μm) and the fine ash fraction ($d_{2\text{-D}} < 63$ μm) of the samples.

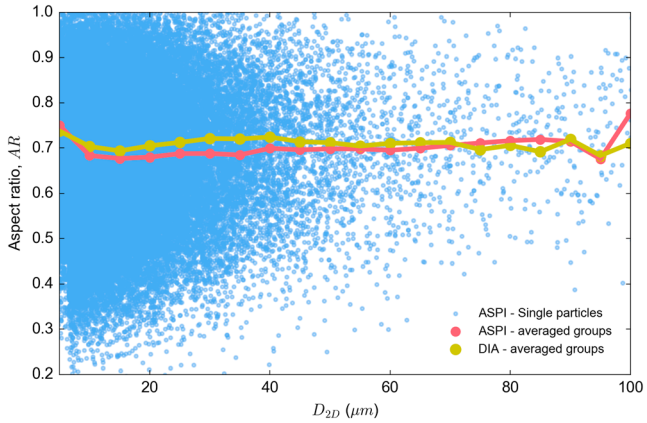

Figure 13. Correlation between the ASPI and the DIA instruments for the calculated aspect ratio of an sample KEL. The blue dots are the single analyzed particles measured by the ASPI, and the red line is the corresponding averaged aspect ratio. The yellow line indicates the mean aspect ratio measured by DIA over the same size range.

represents the averaged shape parameter, where the error bars indicate the variability among the samples. For presenting the data, we formed size bins with 5 μm intervals indicated by the markers, where the first marker indicate the 1.5–5 μm bin, the second marker the range between 5–10 μm, 10–15 μm, etc. Although the fine and coarse ash fractions of the aspect ratio and the Wilson shape parameter show almost no difference, different particle size classes can have different shapes. The two shape parameters first decrease with size, before they increase again at around 10 μm. The Wilson shape parameter is thereby less size sensitive than the aspect ratio and also shows the smallest variability among all samples as indicated by the error bars. The Cox circularity, however, shows a continuous decrease with increasing particle size over the entire size range.

Noticeable is also that the smallest particles (first few μm), for all shape parameters, show higher values (close to 1) than the rest of the data. To confirm this result and to exclude instrumental artifacts, we additionally analyzed samples with a 50X magnification objective lens, designed for the size range of 0.5–40 μm, to see if the particle shape behavior within this size range is the same as obtained with the 20X magnification objective. We found no difference and observed that the shape trend continued in the <1 μm range (indicated by the dashed lines in Figure 14).

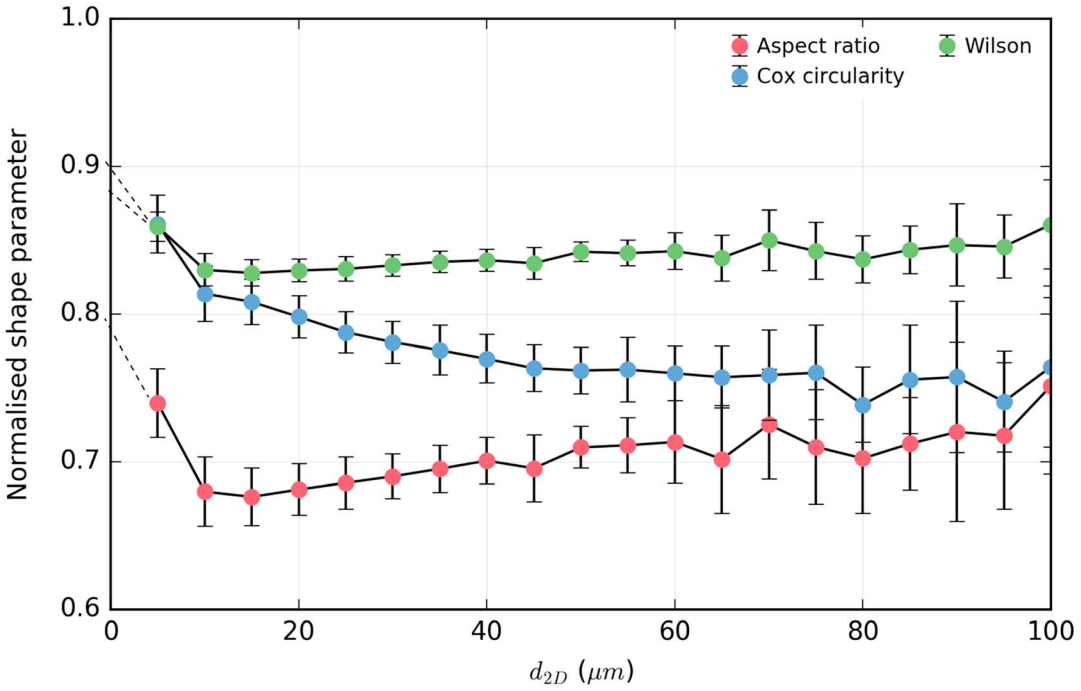

Figure 14. Shape parameters plotted as a function of the particle diameter ($d_{2\text{-}D}$) in the size range between 0.5 and 100 μm. Shape parameters are averaged over 5 μm size bins using data from all analyzed particle samples. The variation of the parameter values is indicated by the standard deviation.

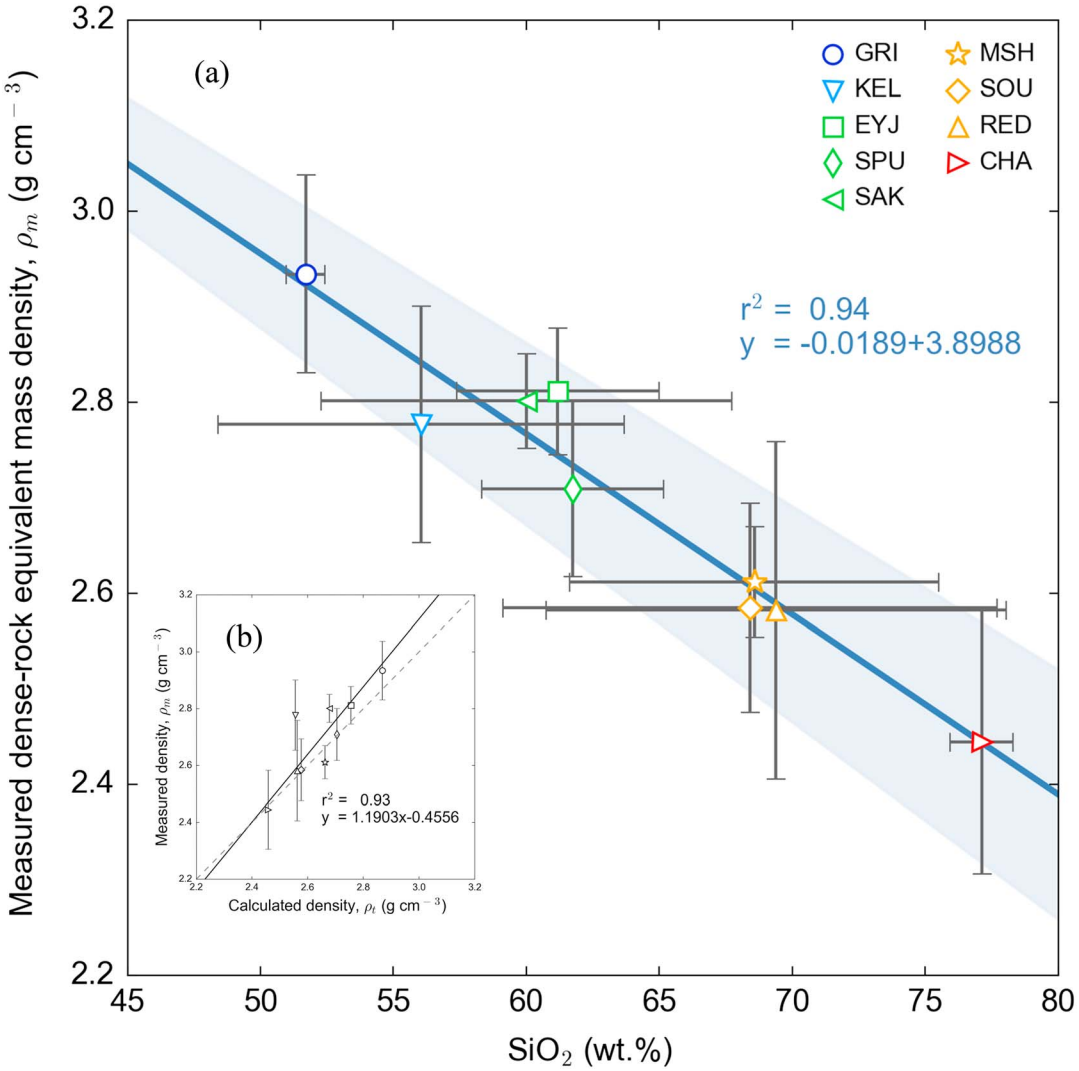

Figure 15. (a) Measured mass density versus SiO_2 content as a predominant fraction of the overall bulk-chemical composition measured by EDS and (b) measured mass density versus mass density derived from the measured chemical composition. The solid lines show the regression functions between the values, whereas the dashed line in (b) represents the 1:1 line. The shaded area in Figure 15a indicates the 1-sigma range of the correlation between the measured mass density and the SiO_2 content.

As a general validation of the measured size and shape parameters obtained by ASPI and to eliminate potential measurement artifacts, we repeated the analysis with a second instrument (DIA) that measured the same parameters. Figure 13 shows, as an example, the correlation between the ASPI and the DIA instruments for the calculated aspect ratio for the sample KEL. The blue dots indicate single analyzed particles measured by the ASPI. The red line illustrates the corresponding averaged aspect ratios resulting from the average of the single point measurements. The yellow line indicates the aspect ratio over the same size range measured by DIA. The correlation of the two data sets shows a good agreement between the two instruments and thus confirms the measured shape trends by the ASPI. Moreover, the measurements by the DIA also confirm the increase of the shape parameter in the size range between 0.5 and 5 μm (first marker).

3.5. Mass Density

Figure 15a shows the correlation of the DRE density measured by Archimedean densitometry and the SiO_2 content obtained by EDS. We used the SiO_2 content, as a predominant and representative component in

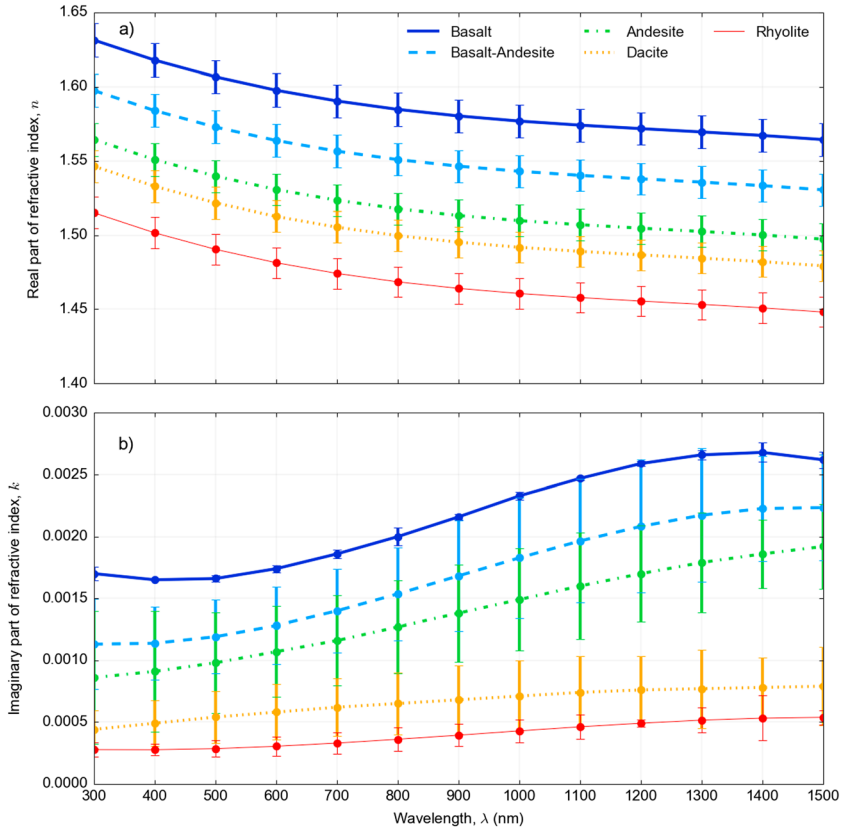

Figure 16. Overview about (a) the real part, calculated with the theoretical arc fusion method [*Church and Johnson*, 1980] in combination with Sellmeier dispersion formulas for the measured chemical compositions, and (b) the imaginary part based on direct spectrophotometer measurements of the complex refractive index sorted into the different igneous rock groups for basaltic (dark blue), basaltic-andesitic (blue), andesitic (green), dacitic (orange), and rhyolitic (red) ash types. Note that the calculated and measured values are plotted at high spectral resolution, but for a better orientation the standard deviation of each sample group is plotted only at 100 nm intervals (circles).

each sample with more than 50 wt %, to correlate the measured density with the chemical composition. The resulting regression function ($y = -0.0189 + 3.8988$) and the 1-sigma ranges, indicated by the blue line and the blue shaded area in Figure 15a, respectively, illustrate that the DRE density decreases with increasing SiO_2 content ($r^2 = 0.94$). The scatter of the data results from uncertainties of both the measured density, the vesicularity, and of the measured composition. The resulting measurement uncertainty range is between 10.3 and 19.34% for KEL and RED, respectively.

For a consistency check of the measured mass density data, we also calculated the density based on the major oxides weight fractions as obtained from the compositional analysis (EDS). The correlation in Figure 15b shows that both approaches give similar results with values around the 1:1 line and a high correlation coefficient ($r^2 = 0.93$; the black solid line represents the resulting linear regression, $y = 1.1903x - 0.4556$). However, all values lie within the uncertainties of the measurements that originate mainly from the small variability of chemical composition and vesicularity within the ash samples.

According to the igneous rock classification, we calculated average density values based on the regression function obtained by the correlation of the SiO_2 content and the measured mass density. Hence, the density including their standard deviation ($\mu \pm \sigma$ in g/cm^3) for basaltic, basaltic-andesitic, andesitic, dacitic, and rhyolitic ashes are $\rho = 2.98 \pm 0.04$, 2.87 ± 0.03, 2.77 ± 0.03, 2.65 ± 0.03, and 2.49 ± 0.06 g/cm^3, respectively (Table 5).

3.6. Complex Refractive Index

We obtained complex refractive index data in the wavelength range between $\lambda = 300$ and 1500 nm. We used the combination of a theoretical arc function method and Sellmeier dispersion equations to derive the scattering properties in a chemical and theoretical description as shown in Figure 16a. Values for the standard

deviation of the data were calculated using the reported uncertainties (±0.007) of the single-point refractive index calculation. Since these data are based on theoretical calculations, the distribution over the wavelength range of these data are very similar. However, the data show that the n_λ are highest in the UV range and decrease with wavelength.

For a systematic representation of these data, we used the chemical composition of our samples, obtained by EDS, to group the nine different samples according to their SiO_2 and total alkali contents into the five main igneous rock groups. The data illustrate the strong dependence of the scattering part on the chemical composition of the samples. The lowest scattering values were found for the highest SiO_2 content ash type (rhyolitic ash) with values between $n_\lambda = 1.38$ for 1500 nm and $n_\lambda = 1.53$ for 300 nm wavelengths, whereas the highest values were found for the lowest SiO_2 content (basaltic ash) with values between $n_\lambda = 1.50$ for 1500 nm and $n_\lambda = 1.66$ for 300 nm. The other ash types (basaltic-andesitic to dacitic ash) lie between the basaltic and rhyolitic ash types according to their chemical compositions.

For the determination of k_λ, we did not find any systematic differences between the 1 vol % and 5 vol % samples. Therefore, we first averaged the data from the 1 and 5 vol % pellet samples and, secondly, averaged the measurement data for samples in each group according to the igneous rock classification. Different to the trend for n_λ, the values for k_λ are lower in the UV-range and increase with wavelength due to the presence of wide absorption bands in the NIR, varying in intensity from different ash types and thus with the chemical compositions. The lowest absorption values were found for the highest SiO_2 ash type (rhyolitic ash) with values between $k_\lambda = 0.00028$ for $\lambda = 300$ nm to $k_\lambda = 0.00054$ for $\lambda = 1500$ nm wavelengths, whereas the highest values were found for the lowest SiO_2 content (basaltic ash) with values between $k_\lambda = 0.00165$ for $\lambda = 300$ nm to $k_\lambda = 0.00268$ for 1500 nm wavelengths. Like in the scattering regime, the other ash types (basaltic-andesitic to dacitic ash) lie between the basaltic and rhyolitic ash types according to their chemical compositions. The samples with the smallest variation in chemical composition showed also the smallest variation in absorptivity.

4. Discussion

4.1. Particle Composition

Chemical composition forms the basis of volcanic ash classification [*Le Bas and Streckeisen*, 1991] and has a fundamental influence on other parameters such as the mass density or the optical properties. The deviation in composition in the intermediate range (basaltic-andesitic to dacitic ash) as shown in Figure 7 can be the result of several processes such as fractional crystallization of a mafic parent magma, partial melting of crustal material, or magma mixing between felsic rhyolitic and mafic basaltic magmas in a magma reservoir. Our measured compositions of the individual ash sample are confirmed by earlier studies where the same samples were already analyzed and their compositions determined [e.g., *Bayhurst et al*., 1994; *Adams et al*., 1996; *McGimsey et al*., 2001; *Alfano et al*., 2011; *Gislason et al*., 2011; *Cole et al*., 2015].

The ratios between the particle bulk and surface composition (oxides in wt %) are shown in Figure 9. The SiO_2 ratios show an overall behavior, where there is a 1:1 surface to volume compositional ratio or a surface enrichment in SiO_2. This is reasonable if we consider that most of the bulk composition consists of SiO_2 and most of the fracture and therefore surface formation originates in the amorphous silicate phase. Another feature is that Ca, Mg, Na, and K ratios follow overall similar trends and are slightly depleted in most ash surfaces as reported by *Delmelle et al*. [2007], *Ayris and Delmelle* [2012], and *Barone et al*. [2014]. We found also a smaller Fe concentration in the particle surface than in the particle bulk but less pronounced than shown by *Delmelle et al*. [2007]. The depletion of these substances on the particle surface may result from either dissolution of an external layer by corrosive mixed gaseous/aqueous fluids (with, e.g., H_2S, SO_2, HCl, HF, HBr, or H_2SO_4 forming acidic conditions) or from gaseous fluorine metasomatism at high temperature [*Delmelle et al*., 2007; *Barone et al*., 2014]. Acidic conditions could promote dissolution of the basic FeO, CaO, and MgO oxides and formation of soluble salts, which can be washed away by water. The Al_2O_3 ratios show the smallest variation. All values lie around the 1:1 ratio line. The small deviations may originate from either Al_2O_3 participating in the silicate phase or also in other crystalline oxide phases. TiO_2 ratios follow the trend of FeO as these two oxides coexist in the same mineral phases titan magnetite (Fe_2TiO_4) and ilmenite ($FeTiO_3$) [*Ayris and Delmelle*, 2012].

Table 3. Comparison of Glass Contents Between This Study and Available Literature Values for Volcanic Glasses of the Same Eruption

		This Study	Reference	
Volcano	Eruption Date	Glass Content (%)	Glass Content (%)	
Mount St.Helens	1980	70.0	72.0	*Blundy and Cashman* [2001]
Redoubt	1989	69.5	69.2	*Nye et al.* [1994]
Spurr	1992	57.6	64.5[a]	*Keith* [1995]
Chaiten	2008	72.1	76.1	*Castro and Dingwell* [2009]
Eyjafjallajökull	2010	54.2	61.8[b]	*Sigmarsson et al.* [2011]
Grímsvötn	2011	50.9	50.6	*Sigmarsson et al.* [2013]

[a]Averaged glass content, range 60–69%.
[b]Averaged glass content, range 59.5–65.5%.

Our glass content data show a good correlation with available literature on the same volcanic eruptions and samples (Table 3). The variation between the values result from differences in sample collection (time and location), applied measurement technique and number of analyzed samples. In the case of our light microscope image analyses, the uncertainties result from manual thresholding (contrast between some particles and the background was too low), and in some cases crystalline particles were present on top of amorphous phases and were taken as crystalline phases only. However, the deviation between the literature values and our values are in the range of 12% and therefore within the error bars of our sample measurements. An comprehensive overview of the glass contents of ash from various eruptions is summarized in *Cashman and Rust* [2016] (Figure 2 and table in the supporting information).

4.2. Particle Physical Properties

Improved knowledge about the microphysical properties of the fine ash fraction is important to investigate atmospheric transport and remote sensing measurements of volcanic ash clouds [*Riley et al*., 2003]. The size and shape controls particle aerodynamic parameter such as the drag coefficient and the terminal velocity of the particles, whereas the mass density also influences gravitational settling and is important to calculate ash mass loadings and mass concentrations from observed particle volume distributions.

The applied 2-D measurement approach is a simplified particle characterization method that provides reliable and accurate particle size and shape information [*Leibrandt and Le Pennec*, 2015; *Liu et al*., 2015]. Compared to very precise, but costly 3-D measurement methods as described by *Bagheri and Bonadonna* [2016a], the 2-D measurements are faster to acquire without losing accuracy when a sufficient number of single particles is investigated [*Bagheri et al*., 2015].

Our particle shape results show that the different shape parameters have a clear dependency on the individual particle sizes (Table 4). This size dependency was consistent in all nine ash samples investigated in this study. The shape parameter show thereby different trends with increasing particle size. Furthermore, findings by *Riley et al*. [2003] and *Mills and Rose* [2010] confirm our results, as they found the same shape trend with changing particle size, including the increase of shape parameter values for the smallest particle sizes (<5 μm) as shown in Figure 14 for the their Mount Spurr and Fuego ash samples. The measurement with an independent instrument (DIA) supports this result.

Particle DRE mass density is an important parameter for both the atmospheric transport of VA particles and to calculate their mass loadings from volume measurements. Our investigated values lie all in the reported mass density range for glass shards, lithic fragments, and crystalline minerals [*Shipley and Sarna-Wojcicki*, 1983] and show that the DRE density can be clearly specified for each of the main igneous rock groups. In many atmospheric related studies, the density is chosen rather arbitrarily due to a lack of reported direct measurements. For example, during the 2010 Eyjafjallajökull eruption, values between ρ = 2.4 g/cm^3 [*Gudmundsson et al*., 2012] and ρ = 3.0 g/cm^3 [*Stohl et al*., 2011] were used. Our data show a good agreement with DRE density values reported by *Bonadonna et al*. [2011] for trachy-andesitic Eyjafjallajökull ash samples (ρ = 2.74 g/cm^3) and by *Eychenne and Le Pennec* [2012] for andesitic Tungurahua ash samples (ρ = 2.68 g/cm^3). DRE mass density values reported by *Pistolesi et al*. [2014] for dacitic-rhyolitic Cordón Caulle ash samples (ρ = 2.69 g/cm^3) are slightly higher, but still within our 1-sigma range. The only reported value in the literature for direct

Table 4. Summary of the Shape Parameter of Analyzed Volcanic Ash Particles[a]

CE Diameter	Aspect Ratio	Cox Circularity	Wilson SP
$d_{CE} = \sqrt{\frac{4A}{\pi}}$	$AR = \frac{d_{l\_axis1}}{d_{l\_axis2}}$	$\phi = \frac{4\pi A}{P^2}$	$WSP = \frac{(b+c)}{2a}$
(μm)	$(\mu \pm \sigma)$	$(\mu \pm \sigma)$	$(\mu \pm \sigma)$
5	0.740 ± 0.023	0.859 ± 0.010	0.859 ± 0.010
10	0.680 ± 0.024	0.830 ± 0.011	0.830 ± 0.011
15	0.676 ± 0.020	0.828 ± 0.009	0.828 ± 0.009
20	0.681 ± 0.017	0.829 ± 0.008	0.829 ± 0.008
25	0.686 ± 0.018	0.831 ± 0.008	0.831 ± 0.008
30	0.690 ± 0.015	0.833 ± 0.007	0.833 ± 0.007
35	0.695 ± 0.016	0.835 ± 0.007	0.835 ± 0.007
40	0.701 ± 0.016	0.836 ± 0.007	0.836 ± 0.007
45	0.695 ± 0.023	0.834 ± 0.011	0.834 ± 0.011
50	0.710 ± 0.014	0.842 ± 0.007	0.842 ± 0.007
55	0.711 ± 0.019	0.841 ± 0.009	0.841 ± 0.009
60	0.713 ± 0.028	0.843 ± 0.012	0.843 ± 0.012
65	0.702 ± 0.036	0.838 ± 0.016	0.838 ± 0.016
70	0.725 ± 0.037	0.850 ± 0.021	0.850 ± 0.021
75	0.710 ± 0.039	0.843 ± 0.019	0.843 ± 0.019
80	0.702 ± 0.037	0.837 ± 0.016	0.837 ± 0.016
85	0.712 ± 0.031	0.844 ± 0.016	0.844 ± 0.016
90	0.720 ± 0.061	0.847 ± 0.028	0.847 ± 0.028
95	0.718 ± 0.050	0.846 ± 0.021	0.846 ± 0.021
100	0.751 ± 0.060	0.861 ± 0.030	0.861 ± 0.030
Total	0.706 ± 0.019	0.840 ± 0.009	0.840 ± 0.009
Fine fraction	0.698 ± 0.017	0.884 ± 0.016	0.837 ± 0.008
Coarse fraction	0.720 ± 0.015	0.867 ± 0.007	0.847 ± 0.007

[a]Shown are the mean values of each size class (e.g., 1.5–5, 5.01–10, and 10.1–15 μm) including the standard deviation for the corresponding classes in the size range between 5 and 100 μm for the shape parameter aspect ratio, Cox circularity, and Wilson shape parameter.

DRE density measurements, conducted by *Rocha-Lima et al.* [2014] for andesitic Eyjafjallajökull ash (ρ = 2.16 g/cm^3), is the only data that do not correlate with our finding and other findings by *Bonadonna et al.* [2011] for the same eruption. But they are even smaller than the density of pure glass shards (ρ = 2.35–2.45 g/cm^3) [*Wilson et al.*, 2012], which is difficult to understand.

4.3. Particle Optical Properties

In the literature, only a small number of studies investigated the optical properties of volcanic ash particles and half of the studies measured the absorption part of the complex refractive index only (as illustrated in Figure 2 and references therein). To place our results into the context of existing data sets, we compared our data with values from *Ball et al.* [2015] (Ba15) for the wavelengths λ = 450, λ = 546 and λ = 650 nm and *Pollack et al.* [1973] (Po73) for the scattering part (Figure 17), and with values from *Ball et al.* [2015], *Pollack et al.* [1973], *Rocha-Lima et al.* [2014] (Ro14), and *Patterson et al.* [1983] (Pa83) for the absorption part (Figure 18). For a better comparability of the different data sets, we grouped the literature data also according to the reported chemical composition, into the igneous rock groups, where the colors in Figures 17 and 18 correspond to the colors used in the SiO_2 and total alkali International Union of Geological Sciences (IUGS) classification (Figure 7). The dashed line in each plot indicates the 1:1 line. Note that according to the IUGS classification, the chemical composition of the Po73 "andesite" sample

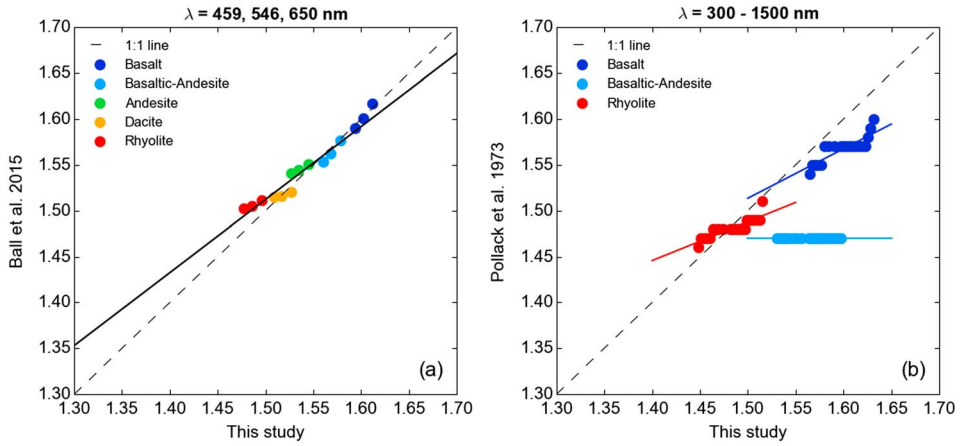

Figure 17. Correlation of calculated real part data of complex refractive index with data from the literature: (a) *Ball et al.* [2015] for the wavelengths 450, 546, and 650 nm and (b) *Pollack et al.* [1973] for the wavelength range between 300 and 1500 nm.

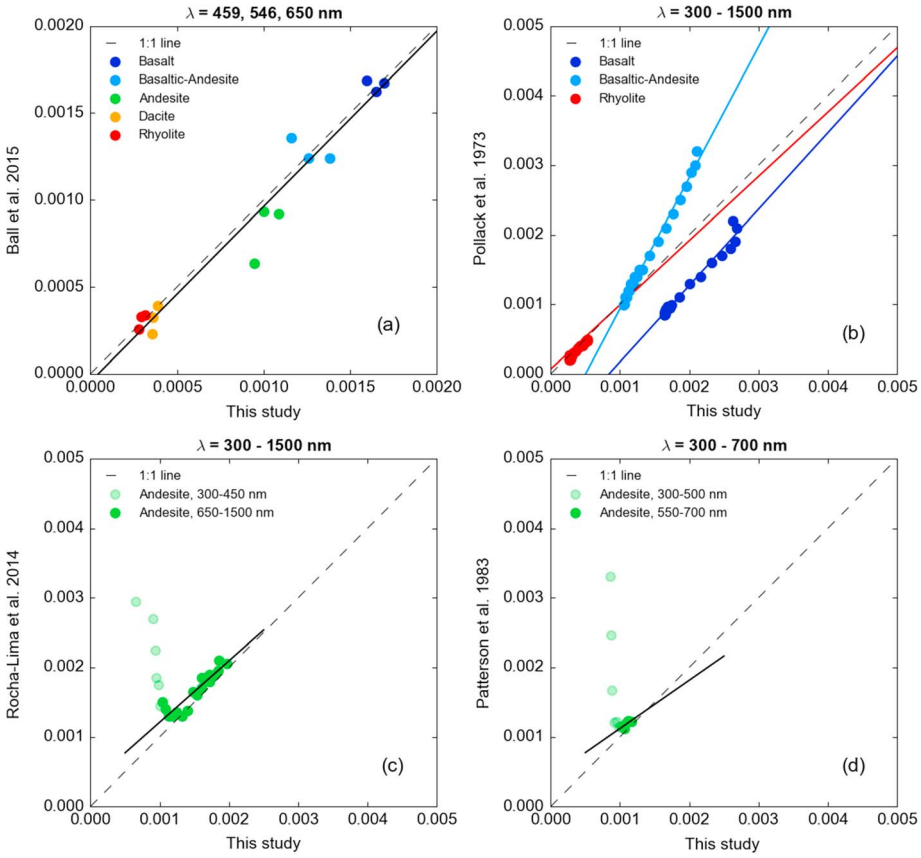

Figure 18. Correlation of measured imaginary part data of refractive index with data from the literature. Correlation with data from (a) *Ball et al.* [2015] for the wavelengths 450, 546, and 650 nm; (b) *Pollack et al.* [1973] for the wavelength range between 300 and 1500 nm; (c) *Rocha-Lima et al.* [2014] for the wavelength range between 350 and 1500 nm; and (d) *Patterson et al.* [1983] for the wavelength range between 300 and 700 nm.

corresponds to basalt-andesite and not andesite. Thus, we compared the Po73 "andesite" with our basalt-andesite values. The calculated values for the scattering part show a good agreement (r^2 = 0.97) with the Ba15 data (for all ash types; Figure 17a), measured with the Becke line method. The scattering data for the basaltic and the rhyolitic ash types in Po73 (Figure 17b) show a good agreement to our data (r^2 = 0.78 and 0.74, respectively), where both data sets reveal a similar trend with higher values in the UV range and a decrease with increasing wavelength but with less variations in the Po73 data. However, no correlation was found for the basalt-andesitic ash type. One potential reason for this could be that the Po73 data show no variability over the wavelength range. No other data set in the literature shows a similar trend with no variation of n_λ in the UV/Vis wavelength range.

The comparison of the measured absorption part data is shown in Figure 18, where our data are compared to other direct transmittance measurements (Figures 18a and 18b) as well as to calculated absorption part data from optical reflectance measurements (Figures 18c and 18d). Dependent on the techniques used to derive the absorption properties, the agreement of the data can vary especially in the UV range. The correlation to the direct transmittance measurements shows a good agreement. For Ba15 the data lie very close to the 1:1 line (r^2 = 0.96). The correlation to the Po73 values shows no clear trend with a very low covariation. Our data are higher for the basaltic sample, lower for the basalt-andesitic ash type, and nearly the same for the rhyolitic ash type. The absorption part data obtained by the indirect measurement methods (scattering data were converted to absorption using the Kubelka-Munk theory) show both the same pattern. The values are much higher (light green dots in Figures 18c and 18d) in the UV range ($\lambda < 500$ nm) and show a decrease with increasing wavelength before they increase again. We find no correlation when we compare our data to all data points (wavelength range between λ = 300 and λ = 1600 nm) shown in Figures 18c and 18d. However, if we compare our data with those of Ro14 and Pa84 only in the wavelength range between

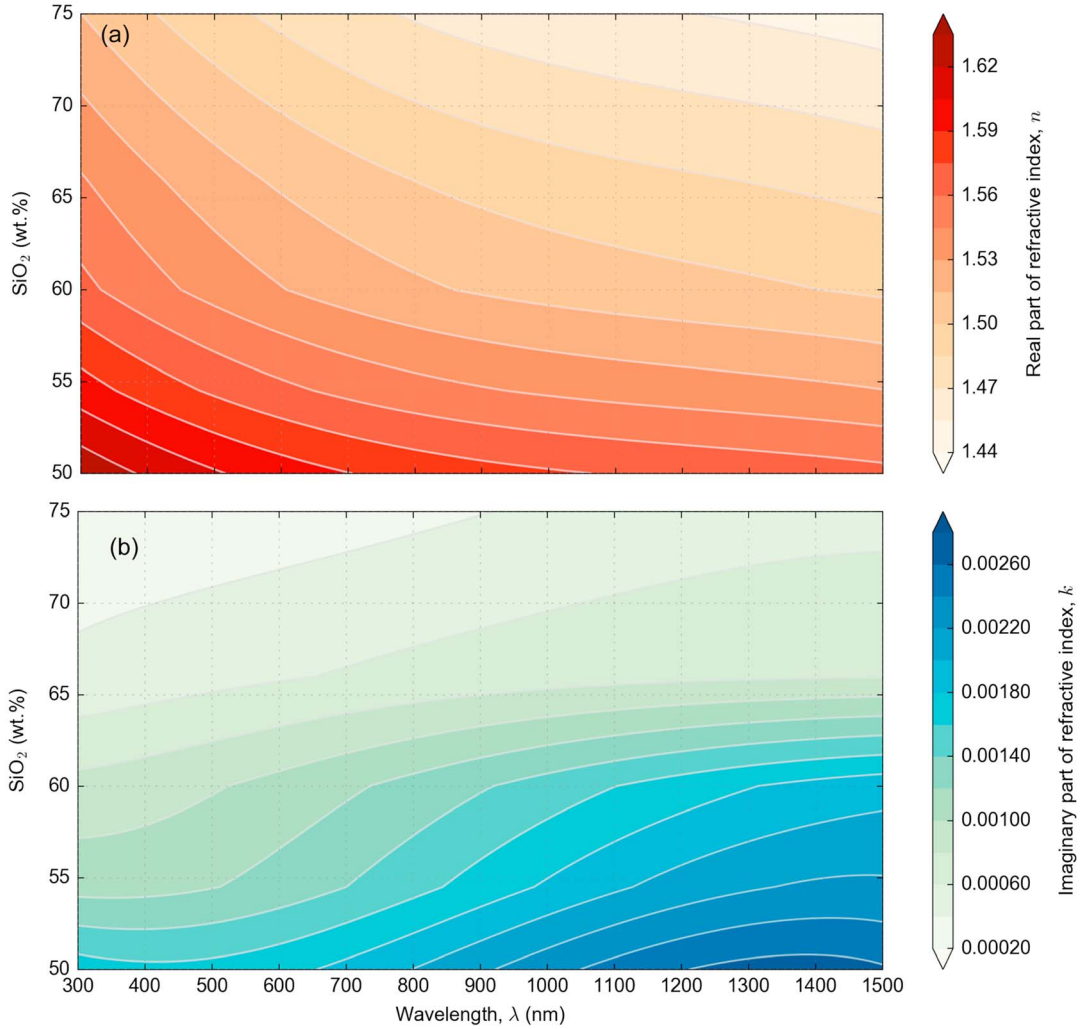

Figure 19. Contour plots of (a) the calculated real part and (b) the measured imaginary part of the complex refractive index as function of the silica content (50–75 wt %) and the spectral wavelength in the range between λ = 300 and λ = 1500 nm. The contour plots are based on the data shown in Figure 16.

λ = 500 and λ = 1500 nm, we see a very good correlation with r^2 = 0.84 and 0.6, respectively. Independent of the deployed measurement technique in all studies and given the high variability in the chemical composition of the individual samples, our results show reassuring conformity to existing literature values (Figures 17 and 18).

The striking feature in all data sets (our data and available literature values), both for *n* and k, is the clear relation between high *n* and *k* values for low SiO_2 contents and low values for high SiO_2 contents (in UV/Vis/NIR range). We summarized these findings in Figure 19 and in Table 5. The plot shows the real part (Figure 19a) and the imaginary part (Figure 19b) of the complex RI as a function of both the spectral wavelength and the SiO_2 content (as a representation of the different chemical compositions) of the ash. These plots can be used to get direct information of the RI for different instruments such as lidars, optical particle counters (OPCs), or satellite instruments (knowing their specific wavelength for the detection of VA), when only the SiO_2 content of the magma is known.

4.4. Broader Context and Application of Data Set

This study presents for the first time a detailed data set that investigated a wide range of volcanic ash particle properties for different volcanic ash types combined in one study. We placed our data in the context of existing data from other studies and combined them in this data set. Improved knowledge of the investigated

Table 5. Summary of the Microphysical and Optical Properties of Volcanic Ash Particles Classified Into the Main Igneous Rock Types[a]

Igneous Rock Types	SiO_2 (wt % ± σ)	Total Alkali (wt % ± σ)	Mass Density $\mu \pm \sigma$ (g/cm^3)	Refractive Index Range (λ = 300–1500 nm)	
				n_λ	k_λ
Basalt	48.5 ± 3.5	2.5 ± 2.5	2.98 ± 0.038	1.50–1.66	0.00165–0.00268
Basalt-andesite	54.5 ± 2.5	2.9 ± 2.9	2.87 ± 0.027	1.46–1.62	0.00113–0.00224
Andesite	60.0 ± 3.0	3.3 ± 3.3	2.77 ± 0.032	1.43–1.58	0.00086–0.00192
Dacite	66.0 ± 3.0	3.7 ± 3.7	2.65 ± 0.032	1.41–1.57	0.00044–0.00079
Rhyolite	75.0 ± 6.0	7.0 ± 7.0	2.49 ± 0.060	1.38–1.53	0.00027–0.00054

[a]For each group the averaged SiO_2 and total alkali contents, the measured mass densities, and complex refractive indices for the wavelength range between 300 and 1500 nm are shown.

properties are relevant for the detection and forecasting of volcanic ash clouds as well as the estimation of their potential impacts on climate, aviation, and human health. Thus, this data set can contribute to minimize uncertainties in the calculation and detection of ash clouds for future or historic volcanic eruptions even when only information about the magma composition is available. We make all data used to generate figures and tables available (see the supporting information), and we hope that our data set can serve as a reference for future studies requiring information on volcanic ash properties.

5. Conclusions

In this paper, we determined the physical, chemical, and optical properties of a representative selection of fine ash samples ($d < 63$ μm) from nine different volcanoes and volcanic eruptions. We used different measurement techniques (image analysis, Archimedean densitometry, energy dispersive, X-ray photoelectron, and UV/Vis/IR spectroscopies) and theoretical methods to obtain the particle bulk and surface chemical composition, the particle size and morphology, DRE mass density, and the spectral complex refractive index.

EDS and XPS measurements showed that the particle bulk and surface have comparable chemical compositions for most of the elements and that all ash samples could be clearly classified into one of the main igneous rock type groups according to their SiO_2 and total alkali contents. Thus, the nine VA samples cover a wide range of SiO_2 contents ranging from basalt (~50 wt % SiO_2) to ehyolite (~80 wt % SiO_2). The analysis of the particle cross section returned stable and reproducible data on the chemical composition that plays a key role in governing the mass density and the complex refractive index. Comparing the bulk composition with the composition of the particle surface (2 to 10 nm depth), we found—despite the overall similarities—also notable differences between the surface and bulk chemical composition. The elements Ca, Na, Mg, and Fe ratios showed slightly higher concentrations in the bulk material compared to the surface, whereas Si was enriched on the surface due to a potential dissolution of an external layer by corrosive mixed gaseous/aqueous fluids.

The light microscopy measurement showed that the glass content can vary from the bulk SiO_2 content. We also found that the glass content within each igneous rock groups can vary significantly especially in the andesite and dacite region.

From the static and dynamic particle imaging measurements, we found that the particle morphology depends systematically on the particle size (in the size range $d_{2\text{-}D} < 100$ μm), and this finding was consistent over the entire sample set. The aspect ratio and the Wilson shape parameter, as measures of particle elongation, showed no significant difference between fine and coarse ashes, whereas the Cox circularity, the measure of the particle roundness, showed significant differences. The overall shape parameters for the fine ash fraction are 0.71, 0.84, and 0.85 for the aspect ratio, the Cox circularity, and the Wilson shape parameter, respectively, and for the coarse ash fraction ($d > 63$ μm) corresponding values are 0.72, 0.74, and 0.84. This consistent pattern in the shape parameters can be used to parameterize the particle shape in ash transport and dispersion, climate, or theoretical terminal velocity calculation models. The DRE mass density, as obtained from Archimedean densitometry and theoretical calculations, shows a clear dependency on the individual chemical composition of the samples and decreases with increasing SiO_2 content. Thus, the

DRE mass density was found to be in the range from ρ = 2.49 ± 0.06 g/cm^3 for rhyolitic ashes to ρ = 2.98 ± 0.04 g/cm^3 for basaltic ashes.

The complex refractive index over a wide wavelength range (λ = 300 to 1500 nm) was analyzed for the first time for a wide silica range and for a high number of different ash samples. We found that the RI shows a clear dependency on the individual chemical composition of the samples, and especially on the SiO_2 content, which could be shown after applying the IUGS chemical classification, both for our data and for data from the literature. This allowed us to connect the wavelength-dependent RI values directly with the SiO_2 contents. Modeled values for the real part, n_λ, obtained by a combination of the arc-function method and the Sellmeier semiempirical link between refractive index and the chemical composition of the ashes, returned results that agree well with available literature values. We found a decrease of values with increasing wavelength, where the ash with the highest SiO_2 content had the highest n_λ value. For the imaginary part, k_λ, obtained by the spectrophotometer measurements, we found that the values increase with increasing wavelength, where basaltic, basaltic-andesitic, and andesitic showed stronger dependency on wavelength, due to a higher potential to absorb light. The dacitic and rhyolitic ash types showed only small absorption properties.

The data set could be further extended by future studies if more data are added to groups with limited samples (basalt, basaltic-andesite, and rhyolite) or where no samples are available (e.g., trachyte, phonolite, and foidite). Comparison of our bulk material results with pure glass components of the same ash samples would be very helpful for a better understanding of the relation between refractive index and composition. Finally, measurements of the optical properties of VA in the near-infrared to the infrared spectral range (λ = 1.5–20 μm) would be useful for infrared remote sensing algorithms.

Acknowledgments

A. Vogel is fully supported by the VERTIGO (Volcanic ash: field, experimental and numerical investigations of processes during its lifecycle) Marie Curie Initial Training Network, funded through the European Seventh Framework Program (FP7 2007-2013) under grant agreement number 607905. A. Stohl was supported by Nordforsk in the frame of the Nordic Center of Excellence eSTICC (eScience Tools for Investigating Climate Change in northern high latitudes) under grant 57001. The contribution of C. Bonadonna was supported by the Swiss National Science Foundation project 200021_156255. The authors thank the mentioned working groups for sampling and supplying the ash samples and G. Bagheri for discussions and his feedback about the physical characterization of the samples. We also thank Joachim Seland Graff for his support and assistance in the SINTEF Materials and Chemistry characterization laboratory and the three anonymous reviewers for their suggestions and comments. The data used to generate figures and tables in this paper are available in the supporting information.

References

Achterberg, E. P., et al. (2013), Natural iron fertilization by the Eyjafjallajökull volcanic eruption, *Geophys. Res. Lett.*, *40*, 921–926, doi:10.1002/grl.50221.

Adams, R. J., W. F. Perger, W. I. Rose, and A. Kostinski (1996), Measurements of the complex dielectric constant of volcanic ash from 4 to 19 GHz, *J. Geophys. Res.*, *101*, 8175–8185, doi:10.1029/96JB00193.

Alfano, F., C. Bonadonna, A. C. M. Volentik, C. B. Connor, S. F. L. Watt, D. M. Pyle, and L. J. Connor (2011), Tephra stratigraphy and eruptive volume of the May, 2008, Chaiten eruption, Chile, *Bull. Volcanol.*, *73*(5), 613–630, doi:10.1007/s00445-010-0428-x.

Ayris, P., and P. Delmelle (2012), Volcanic and atmospheric controls on ash iron solubility: A review, *Phys. Chem. Earth*, *45–46*, 103–112, doi:10.1016/j.pce.2011.04.013.

Bagheri, G., and C. Bonadonna (2016a), Chapter 2—Aerodynamics of volcanic particles: Characterization of size, shape, and settling velocity, in *Volcanic Ash*, pp. 39–52, Elsevier, Amsterdam, Netherlands.

Bagheri, G., and C. Bonadonna (2016b), On the drag of freely falling non-spherical particles, *Powder Technol.*, *301*, 526–544, doi:10.1016/j.powtec.2016.06.015.

Bagheri, G., E. Rossi, S. Biass, and C. Bonadonna (2016), Timing and nature of volcanic particle clusters based on state-of-the-art field and numerical investigations, *J. Volcanol. Geotherm. Res.*, doi:10.1016/j.jvolgeores.2016.09.009.

Bagheri, G. H., C. Bonadonna, I. Manzella, P. Pontelandolfo, and P. Haas (2013), Dedicated vertical wind tunnel for the study of sedimentation of non-spherical particles, *Rev. Sci. Instrum.*, *84*(5), 54501, doi:10.1063/1.4805019.

Bagheri, G. H., C. Bonadonna, I. Manzella, and P. Vonlanthen (2015), On the characterization of size and shape of irregular particles, *Powder Technol.*, *270*(Part A), 141–153, doi:10.1016/j.powtec.2014.10.015.

Ball, J. G. C., B. E. Reed, R. G. Grainger, D. M. Peters, T. A. Mather, and D. M. Pyle (2015), Measurements of the complex refractive index of volcanic ash at 450, 546.7, and 650 nm, *J. Geophys. Res. Atmos.*, *120*, 7747–7757, doi:10.1002/2015JD023521.

Barone, G., E. Ciliberto, P. Costagliola, and P. Mazzoleni (2014), X-ray photoelectron spectroscopy of Mt. Etna volcanic ashes, *Surf. Interface Anal.*, *46*(10–11), 847–850, doi:10.1002/sia.5395.

Baxter, P. J., A. Searl, H. A. Cowie, D. Jarvis, and C. J. Horwell (2014), Evaluating the respiratory health risks of volcanic ash at the eruption of the Soufrière Hills Volcano, Montserrat, 1995–2010, in *The Eruption of Soufrière Hills Volcano, Montserrat from 2000 to 2010*, vol. 39, edited by G. Wadge, R. E. A. Robertson, and B. Voight, *Geol. Soc. London, 39*, 407–425, doi:10.1144/M39.22.

Bayhurst, G. K., K. H. Wohletz, and A. S. Mason (1994), A method for characterizing volcanic ash from the December 15, 1989, eruption of Redoubt Volcano, Alaska, *Volcan. Ash Aviat. Saf. US Geol. Surv. Bull.*, *2047*, 13–18.

Blundy, J., and K. Cashman (2001), Ascent-driven crystallisation of dacite magmas at Mount St Helens, 1980–1986, *Contrib. Mineral. Petrol.*, *140*(6), 631–650, doi:10.1007/s004100000219.

Bonadonna, C., and B. F. Houghton (2005), Total grain-size distribution and volume of tephra-fall deposits, *Bull. Volcanol.*, *67*(5), 441–456, doi:10.1007/s00445-004-0386-2.

Bonadonna, C., and J. C. Phillips (2003), Sedimentation from strong volcanic plumes, *J. Geophys. Res.*, *108*(B7), 2340, doi:10.1029/2002JB002034.

Bonadonna, C., G. G. J. Ernst, and R. S. J. Sparks (1998), Thickness variations and volume estimates of tephra fall deposits: The importance of particle Reynolds number, *J. Volcanol. Geotherm. Res.*, *81*(3–4), 173–187, doi:10.1016/S0377-0273(98)00007-9.

Bonadonna, C., R. Genco, M. Gouhier, M. Pistolesi, R. Cioni, F. Alfano, A. Hoskuldsson, and M. Ripepe (2011), Tephra sedimentation during the 2010 Eyjafjallajkull eruption (Iceland) from deposit, radar, and satellite observations, *J. Geophys. Res.*, *116*, B12202, doi:10.1029/2011JB008462.

Bukowiecki, N., et al. (2011), Ground-based and airborne in-situ measurements of the Eyjafjallajökull volcanic aerosol plume in Switzerland in spring 2010, *Atmos. Chem. Phys.*, *11*(19), 10,011–10,030, doi:10.5194/acp-11-10011-2011.

Carn, S., and N. A. Krotkov (2016), Ultraviolet satellite measurements of volcanic ash, in *Volcanic Ash—Hazard Observation*, edited by S. Mackie et al., pp. 217–231, Elsevier, Amsterdam, Netherlands.

Casadevall, T. J. (1994), The 1989–1990 eruption of Redoubt Volcano, Alaska: Impacts on aircraft operations, *J. Volcanol. Geotherm. Res.*, *62*(1–4), 301–316, doi:10.1016/0377-0273(94)90038-8.

Cashman, K., and A. Rust (2016), Volcanic ash: Generation and spatial variations, in *Volcanic Ash*, edited by S. Mackie et al., pp. 5–22, Elsevier, Amsterdam, Netherlands.

Castro, J. M., and D. B. Dingwell (2009), Rapid ascent of rhyolitic magma at Chaitén Volcano, Chile, *Nature*, *461*(7265), 780–783, doi:10.1038/nature08458.

Church, B. N., and W. M. Johnson (1980), Calculation of the refractive index of silicate glasses from chemical composition, *Bull. Geol. Soc. Am.*, *91*(10), 619–625, doi:10.1130/0016-7606(1980)91<619:COTRIO>2.0.CO;2.

Clarisse, L., and F. Prata (2016), Infrared sounding of volcanic ash, in *Volcanic Ash*, edited by S. Mackie et al., pp. 189–215, Elsevier, Amsterdam, Netherlands.

Cole, P., A. Stinton, H. Odbert, C. Bonadonna, and R. Stewart (2015), An inclined Vulcanian explosion and associated products, *J. Geol. Soc. Lond.*, *172*(3), 287–293, doi:10.1144/jgs2014-099.

Costa, A., G. Macedonio, and A. Folch (2006), A three-dimensional Eulerian model for transport and deposition of volcanic ashes, *Earth Planet. Sci. Lett.*, *241*(3–4), 634–647, doi:10.1016/j.epsl.2005.11.019.

Cox, E. P. (1927), A method of assigning numerical and percentage values to the degree of roundness of sand grains, *SEPM Soc. Sediment. Geol.*, *1*(3), 179–183.

Dellino, P., M. T. Gudmundsson, G. Larsen, D. Mele, J. A. Stevenson, T. Thordarson, and B. Zimanowski (2012), Ash from the Eyjafjallajökull eruption (Iceland): Fragmentation processes and aerodynamic behavior, *J. Geophys. Res.*, *117*, B00C04, doi:10.1029/2011JB008726.

Delmelle, P., M. Lambert, Y. Dufrêne, P. Gerin, and N. Óskarsson (2007), Gas/aerosol-ash interaction in volcanic plumes: New insights from surface analyses of fine ash particles, *Earth Planet. Sci. Lett.*, *259*(1–2), 159–170, doi:10.1016/j.epsl.2007.04.052.

Dingwell, D. B., Y. Lavallée, and U. Kueppers (2012), Volcanic ash: A primary agent in the Earth system, *Phys. Chem. Earth*, *45–46*, 2–4, doi:10.1016/j.pce.2011.07.007.

Duggen, S., N. Olgun, P. Croot, L. Hoffmann, H. Dietze, and C. Teschner (2009), The role of airborne volcanic ash for the surface ocean biogeochemical iron-cycle: A review, *Biogeosci. Discuss.*, *6*(4), 6441–6489, doi:10.5194/bgd-6-6441-2009.

Durant, A. J. (2015), Toward a realistic formulation of fine-ash lifetime in volcanic clouds, *Geology*, *43*(3), 271–273, doi:10.1016/0032.

Durant, A. J., and W. I. Rose (2009), Sedimentological constraints on hydrometeor-enhanced particle deposition: 1992 eruptions of Crater Peak, Alaska, *J. Volcanol. Geotherm. Res.*, *186*(1–2), 40–59, doi:10.1016/j.jvolgeores.2009.02.004.

Durant, A. J., R. A. Shaw, W. I. Rose, Y. Mi, and G. G. J. Ernst (2008), Ice nucleation and overseeding of ice in volcanic clouds, *J. Geophys.*, *113*, D09206, doi:10.1029/2007JD009064.

Durant, A. J., C. Bonadonna, and C. J. Horwell (2010), Atmospheric and environmental impacts of volcanic particulates, *Elements*, *6*(4), 235–240, doi:10.2113/gselements.6.4.235.

Eychenne, J., and J. L. Le Pennec (2012), Sigmoidal particle density distribution in a subplinian scoria fall deposit, *Bull. Volcanol.*, *74*(10), 2243–2249, doi:10.1007/s00445-012-0671-4.

Flanner, M. G., A. S. Gardner, S. Eckhardt, A. Stohl, and J. Perket (2014), Aerosol radiative forcing from the 2010 Eyjafjallajökull volcanic eruptions, *J. Geophys. Res. Atmos.*, *119*, 9481–9491, doi:10.1002/2014JD021977.

Folch, A. (2012), A review of tephra transport and dispersal models: Evolution, current status, and future perspectives, *J. Volcanol. Geotherm. Res.*, *235–236*, 96–115, doi:10.1016/j.jvolgeores.2012.05.020.

Gislason, S. R., et al. (2011), Characterization of Eyjafjallajokull volcanic ash particles and a protocol for rapid risk assessment, *Proc. Natl. Acad. Sci. U.S.A.*, *108*(18), 7307–7312, doi:10.1073/pnas.1015053108.

Gonnermann, H. M., and M. Manga (2003), Explosive volcanism may not be an inevitable consequence of magma fragmentation, *Nature*, *426*(6965), 432–435, doi:10.1038/nature02138.

Grainger, R. G., D. M. Peters, G. E. Thomas, A. J. A. Smith, R. Siddans, E. Carboni, and A. Dudhia (2013), Measuring volcanic plume and ash properties from space, *Geol. Soc. Lond. Spec. Publ.*, *1*, 1–60, doi:10.1144/SP380.7.

Gudmundsson, M. T., et al. (2012), Ash generation and distribution from the April–May 2010 eruption of Eyjafjallajökull, Iceland, *Sci. Rep.*, *2*, 1–12, doi:10.1038/srep00572.

Guffanti, M., T. J. Casadevall, and K. Budding (2010), Encounters of aircraft with volcanic ash clouds: A compilation of known incidents, 1953–2009, *U.S. Geol. Surv. Data Ser.*, *545*(1), 1–12.

Heiken, G. (1972), Morphology and petrography of volcanic ashes, *Bull. Geol. Soc. Am.*, *83*(7), 1961–1988, doi:10.1130/0016-7606(1972)83[1961:MAPOVA]2.0.CO;2.

Horwell, C. J., and P. J. Baxter (2006), The respiratory health hazards of volcanic ash: A review for volcanic risk mitigation, *Bull. Volcanol.*, *69*(1), 1–24, doi:10.1007/s00445-006-0052-y.

Ishimoto, H., K. Masuda, K. Fukui, T. Shimbori, T. Inazawa, H. Tuchiyama, K. Ishii, and T. Sakurai (2016), Estimation of the refractive index of volcanic ash from satellite infrared sounder data, *Remote Sens. Environ.*, *174*, 165–180, doi:10.1016/j.rse.2015.12.009.

Jones, M. T., and S. R. Gislason (2008), Rapid releases of metal salts and nutrients following the deposition of volcanic ash into aqueous environments, *Geochim. Cosmochim. Acta*, *72*(15), 3661–3680, doi:10.1016/j.gca.2008.05.030.

Kandler, K., et al. (2011), Electron microscopy of particles collected at Praia, Cape Verde, during the Saharan Mineral Dust Experiment: Particle chemistry, shape, mixing state and complex refractive index, *Tellus Ser. B Chem. Phys. Meteorol.*, *63*(4), 475–496, doi:10.1111/j.1600-0889.2011.00550.x.

Keith, T. E. C. (1995), *The 1992 Eruptions of Crater Peak Vent*, *Bulletin*, Mount Spurr Volcano, Alaska Bulletin [online] Available from: https://pubs.er.usgs.gov/publication/b2139 (Accessed 24 April 2017).

Krotkov, N. A., A. J. Krueger, and P. K. Bhartia (1997), Ultraviolet optical model of volcanic clouds for remote sensing of ash and sulfur dioxide, *J. Geophys. Res.*, *102*, 21,891–21,904, doi:10.1029/97JD01690.

Krotkov, N. A., D. E. Flittner, A. J. Krueger, A. Kostinski, C. Riley, W. Rose, and O. Torres (1999a), Effect of particle non-sphericity on satellite monitoring of drifting volcanic ash clouds, *J. Quant. Spectrosc. Radiat. Transf.*, *63*(2–6), 613–630, doi:10.1016/S0022-4073(99)00041-2.

Krotkov, N. A., O. Torres, C. Seftor, A. J. Krueger, A. Kostinski, W. I. Rose, G. J. S. Bluth, D. Schneider, and S. J. Schaefer (1999b), Comparison of TOMS and AVHRR volcanic ash retrievals from the August 1992 eruption of Mt. Spurr, *Geophys. Res. Lett.*, *26*, 455–458, doi:10.1029/1998GL900278.

Kylling, A., M. Kahnert, H. Lindqvist, and T. Nousiainen (2014), Volcanic ash infrared signature: Porous non-spherical ash particle shapes compared to homogeneous spherical ash particles, *Atmos. Meas. Tech.*, *7*(4), 919–929, doi:10.5194/amt-7-919-2014.

Lange, R. A., and I. S. E. Carmichael (1987), Densities of Na_2O-K_2O-MgO-MgO-FeO-Fe_2O_3-A I_3O_3-TiO_2-SiO_2 liquids: New measurements and derived partial molar properties, *Geochim. Cosmochim. Acta*, *51*(11), 2931–2946, doi:10.1016/0016-7037(87)90368-1.

Le Bas, M. J., and A. L. Streckeisen (1991), The IUGS systematics of igneous rocks, *J. Geol. Soc. Lond.*, *148*(5), 825–833, doi:10.1144/gsjgs.148.5.0825.

Leibrandt, S., and J. L. Le Pennec (2015), Towards fast and routine analyses of volcanic ash morphometry for eruption surveillance applications, *J. Volcanol. Geotherm. Res.*, *297*, 11–27, doi:10.1016/j.jvolgeores.2015.03.014.

Lieke, K. I., T. B. Kristensen, U. S. Korsholm, J. H. Sørensen, K. Kandler, S. Weinbruch, D. Ceburnis, J. Ovadnevaite, C. D. O'Dowd, and M. Bilde (2013), Characterization of volcanic ash from the 2011 Grímsvötn eruption bymeans of single-particle analysis, *Atmos. Environ.*, *79*, 411–420, doi:10.1016/j.atmosenv.2013.06.044.

Liu, E. J., K. V. Cashman, and A. C. Rust (2015), Optimising shape analysis to quantify volcanic ash morphology, *Geo. Res. J.*, *8*, 14–30, doi:10.1016/j.grj.2015.09.001.

Le Maitre, R. W. (1976), The chemical variabilty of some common igneous rocks, *J. Petrol.*, *17*, 589–637.

McCrone, W. C., L. B. McCrone, and J. G. Delly (1978), *Polarized Light Microscopy*, Ann Arbor Sci. Publ., Inc., Michigan.

McGimsey, R. G., C. A. Neal, and C. M. Riley (2001), *Areal Distribution, Thickness, Mass, Volume, and Grain Size of Tephra-Fall Deposits From the 1992 Eruptions of Crater Peak Vent*, Mt. Spurr Volcano, Alaska.

Mele, D., P. Dellino, R. Sulpizio, and G. Braia (2011), A systematic investigation on the aerodynamics of ash particles, *J. Volcanol. Geotherm. Res.*, *203*(1–2), 1–11, doi:10.1016/j.jvolgeores.2011.04.004.

Mills, O. P., and W. I. Rose (2010), Shape and surface area measurements using scanning electron microscope stereo-pair images of volcanic ash particles, *Geosphere*, *6*(6), 805–811, doi:10.1130/GES00558.1.

Munoz, O., H. Volten, J. W. Hovenier, B. Veihelmann, W. J. van der Zande, L. B. F. M. Waters, and W. I. Rose (2004), Scattering matrices of volcanic ash particles of Mount St. Helens, Redoubt, and Mount Spurr Volcanoes, *J. Geophys. Res.*, *109*, D16201, doi:10.1029/2004JD004684.

Mysen, B. O., and P. Richet (2005), *Silicate Glasses and Melts: Properties and Structure*, Science, Elsevier.

Nobbs, J. H. (1985), Kubelka—Munk theory and the prediction of reflectance, *Rev. Prog. Color. Relat. Top.*, *15*(1), 66–75, doi:10.1111/j.1478-4408.1985.tb03737.x.

Nye, C. J., S. E. Swanson, V. F. Avery, and T. P. Miller (1994), Geochemistry of the 1989–1990 eruption of redoubt volcano: Part I. Whole-rock major- and trace-element chemistry, *J. Volcanol. Geotherm. Res.*, *62*(1–4), 429–452, doi:10.1016/0377-0273(94)90046-9.

Patterson, E. M. (1977), Atmospheric extinction between 0.55 μm and 10.6 μm due to soil-derived aerosols, *Appl. Opt.*, *16*(9), 2414–2418, doi:10.1364/AO.16.002414.

Patterson, E. M. (1981), Measurements of the imaginary part of the refractive index between 300 and 700 nanometers for Mount St. Helens ash, *Science*, *211*(4484), 836–838, doi:10.1126/science.211.4484.836.

Patterson, E. M., C. O. Pollard, and I. Galindo (1983), Optical properties of the ash from El Chichon Volcano, *Geophys. Res. Lett.*, *10*, 317–320, doi:10.1029/GL010i004p00317.

Pistolesi, M., R. Cioni, C. Bonadonna, M. Elissondo, V. Baumann, A. Bertagnini, L. Chiari, R. Gonzales, M. Rosi, and L. Francalanci (2014), Complex dynamics of small-moderate volcanic events: The example of the 2011 rhyolitic Cordón Caulle eruption, Chile, *Bull. Volcanol.*, *77*(1), doi:10.1007/s00445-014-0898-3.

Pollack, J. B., O. B. Toon, and B. N. Khare (1973), Optical properties of some terrestrial rocks and glasses, *Icarus*, *19*(3), 372–389, doi:10.1016/0019-1035(73)90115-2.

Prata, A. J., and A. Tupper (2009), Aviation hazards from volcanoes: The state of the science, *Nat. Hazards*, *51*(2), 239–244, doi:10.1007/s11069-009-9415-y.

Retsch Technology GmbH (2016), Particle analyzer CAMSIZER ® P4 particle size and particle shape analysis with, pp. 1–16. [Available at http://www.horiba.com/fileadmin/uploads/Scientific/Documents/PSA/CAMSIZER_XT_flyer.pdf, (Accessed 29 November 2016).]

Riley, C. M., W. I. Rose, and G. J. S. Bluth (2003), Quantitative shape measurements of distal volcanic ash, *J. Geophys. Res.*, *108*(B10), 2504, doi:10.1029/2001JB000818.

Robock, A. (2000), Volcanic eruptions and climate, *Rev. Geophys.*, *38*, 191–219, doi:10.1029/1998RG000054.

Rocha-Lima, A., J. V. Martins, L. A. Remer, N. A. Krotkov, M. H. Tabacniks, Y. Ben-Ami, and P. Artaxo (2014), Optical, microphysical and compositional properties of the Eyjafjallajökull volcanic ash, *Atmos. Chem. Phys. Discuss.*, *14*(9), 13,271–13,300, doi:10.5194/acpd-14-13271-2014.

Rogers, N., and C. Hawkesworth (2000), Composition of magmas, in *The Encyclopedia of Volcanoes*, edited by S. H. B. Houghton et al., pp. 115–131, Elsevier, London.

Rolf, C., M. Krämer, C. Schiller, M. Hildebrandt, and M. Riese (2012), Lidar observation and model simulation of a volcanic-ash-induced cirrus cloud during the Eyjafjallajökull eruption, *Atmos. Chem. Phys.*, *12*(21), 10,281–10,294, doi:10.5194/acp-12-10281-2012.

Rose, W. I., and A. J. Durant (2009), Fine ash content of explosive eruptions, *J. Volcanol. Geotherm. Res.*, *186*(1–2), 32–39, doi:10.1016/j.jvolgeores.2009.01.010.

Rose, W. I., G. J. S. Bluth, D. J. Schneider, G. G. J. Ernst, C. M. Riley, L. J. Henderson, and R. G. McGimsey (2001), Observations of volcanic clouds in their first few days of atmospheric residence: The 1992 eruptions of Crater Peak, Mount Spurr volcano, Alaska, *J. Geol.*, *109*(6), 677–694, doi:10.1086/323189.

Schneider, D., W. I. Rose, and L. Kelley (1995), *Tracking of 1992 Eruption Clouds From Crater Peak Vent of Mount Spurr Volcano, Alaska, Using AVHRR, 1992 Eruptions Crater Peak Vent*, pp. 27–36, Mt. Spurr Volcano, Alaska.

Schneider, D. J., and W. I. Rose (1994), Observations of the 1989–90 Redoubt Volcano eruption clouds using AVHRR satellite imagery, *U.S. Geol. Surv. Bull.*, *2047*, 405–418. [Available at http://www.scopus.com/inward/record.url?eid=2-s2.0-0028562774&partnerID=40&md5=9ba1d08370c71fa1ae6b0a467b77e605.]

Shipley, S., and A. Sarna-Wojcicki (1983), Distribution, thickness, and mass of late Pleistocene and Holocene tephra from major volcanoes in the northwestern United States: A preliminary assessment of hazards from volcanic ejecta to nuclear reactors in the Pacific northwest, Dep. of the Interior - United States Geol. Surv.

Sigmarsson, O., I. Vlastelic, R. Andreasen, I. Bindeman, J. L. Devidal, S. Moune, J. K. Keiding, G. Larsen, A. Höskuldsson, and T. H. Thordarson (2011), Remobilization of silicic intrusion by mafic magmas during the 2010 Eyjafjallajökull eruption, *Solid Earth*, *2*(2), 271–281, doi:10.5194/se-2-271-2011.

Sigmarsson, O., B. Haddadi, S. Carn, S. Moune, J. Gudnason, K. Yang, and L. Clarisse (2013), The sulfur budget of the 2011 Grímsvötn eruption, Iceland, *Geophys. Res. Lett.*, *40*, 6095–6100, doi:10.1002/2013GL057760.

Sparks, R. S. J. (1978), The dynamics of bubble formation and growth in magmas: A review and analysis, *J. Volcanol. Geotherm. Res.*, *3*(1–2), 1–37, doi:10.1016/0377-0273(78)90002-1.

Stevenson, J. A., S. C. Millington, F. M. Beckett, G. T. Swindles, and T. Thordarson (2015), Big grains go far: Understanding the discrepancy between tephrochronology and satellite infrared measurements of volcanic ash, *Atmos. Meas. Tech.*, *8*(5), 2069–2091, doi:10.5194/amt-8-2069-2015.

Stohl, A., et al. (2011), Determination of time-and height-resolved volcanic ash emissions and their use for quantitative ash dispersion modeling: The 2010 Eyjafjallajökull eruption, *Atmos. Chem. Phys.*, *11*(9), 4333–4351, doi:10.5194/acp-11-4333-2011.

Tesche, M., P. Glantz, C. Johansson, M. Norman, A. Hiebsch, A. Ansmann, D. Althausen, R. Engelmann, and P. Seifert (2012), Volcanic ash over scandinavia originating from the Grimsvotn eruptions in May 2011, *J. Geophys. Res.*, *117*, D09201, doi:10.1029/2011JD017090.

Thorsteinsson, T., T. Johannsson, A. Stohl, and N. I. Kristiansen (2012), High levels of particulate matter in Iceland due to direct ash emissions by the Eyjafjallajkull eruption and resuspension of deposited ash, *J. Geophys. Res.*, *117*, B00C05, doi:10.1029/2011JB008756.

Timmreck, C. (2012), Modeling the climatic effects of large explosive volcanic eruptions, *Wiley Interdiscip. Rev. Clim. Change*, *3*(6), 545–564, doi:10.1002/wcc.192.

Vernier, J.-P., T. D. Fairlie, T. Deshler, M. Natarajan, T. Knepp, K. Foster, F. G. Wienhold, K. M. Bedka, L. Thomason, and C. Trepte (2016), In situ and space-based observations of the Kelud volcanic plume: The persistence of ash in the lower stratosphere, *J. Geophys. Res. Atmos.*, *121*, 11,104–11,118, doi:10.1002/2016JD025344.

Volz, F. E. (1973), Infrared optical constants of ammonium sulfate, Sahara dust, volcanic pumice, and Flyash, *Appl. Opt.*, *12*(3), 564, doi:10.1364/AO.12.000564.

Wadell, H. (1932), Volume, shape, and roundness of rock particles, *J. Geol.*, *40*, 443–451.

Weber, K., J. Eliasson, A. Vogel, C. Fischer, T. Pohl, G. van Haren, M. Meier, B. Grobety, and D. Dahmann (2012), Airborne in-situ investigations of the Eyjafjallajökull volcanic ash plume on iceland and over north-western Germany with light aircrafts and optical particle counters, *Atmos. Environ.*, *48*, 9–21, doi:10.1016/j.atmosenv.2011.10.030.

Weber, M. J. (2003), *Handbook of Optical Materials*, CRC Press LLC, Boca Raton, Fla.

Wen, S., and W. I. Rose (1994), Retrieval of sizes and total masses of particles in volcanic clouds using AVHRR bands 4 and 5, *J. Geophys. Res.*, *99*, 5421–5431, doi:10.1029/93JD03340.

White, J. D. L., and B. F. Houghton (2006), Primary volcaniclastic rocks, *Geology*, *34*(8), 677–680, doi:10.1130/G22346.1.

Wilson, L., and T. C. Huang (1979), The influence of shape on the atmospheric settling velocity of volcanic ash particles, *Earth Planet. Sci. Lett.*, *44*(2), 311–324, doi:10.1016/0012-821X(79)90179-1.

Wilson, T. M., C. Stewart, V. Sword-Daniels, G. S. Leonard, D. M. Johnston, J. W. Cole, J. Wardman, G. Wilson, and S. T. Barnard (2012), Volcanic ash impacts on critical infrastructure, *Phys. Chem. Earth*, *45–46*, 5–23, doi:10.1016/j.pce.2011.06.006.

Zaccanti, G., and P. Bruscaglioni (1988), Deviation from the Lambert-Beer law in the transmittance of a light beam through diffusing media: Experimental results, *J. Mod. Opt.*, *35*(2), 229–242, doi:10.1080/09500348814550281.